WILEY

Computational homogenization of higher-order continua

Felix Schmidt[1] | **Melanie Krüger[1]** | **Marc-André Keip[2]** | **Christian Hesch[1]**

[1]Chair of Computational Mechanics, University of Siegen, Siegen, Germany

[2]Institute of Applied Mechanics, University of Stuttgart, Stuttgart, Germany

Correspondence
Christian Hesch, Chair of Computational Mechanics, University of Siegen, Siegen, Germany.
Email: christian.hesch@uni-siegen.de

Abstract

We introduce a novel computational framework for the multiscale simulation of higher-order continua that allows for the consideration of first-, second-, and third-order effects at both micro- and macro-level. In line with classical two-scale approaches, we describe the microstructure via representative volume elements that are attached at each integration point of the macroscopic problem. To take account of the extended continuity requirements of independent fields at micro- and macro-level, we discretize both scales via isogeometric analysis (IGA). As a result, we obtain an IGA²-method that is conceptually similar to the well-known FE²-method. We demonstrate the functionality and accuracy of this novel multiscale method by means of a series of multiscale simulations involving different kinds of higher-order continua.

KEYWORDS
consistent linearization, energetic criteria, higher-order gradient material, IGA²-method, multigrid, representative volume element

1 | INTRODUCTION

Whether or not morphological features of a material are visible depends on the observed length scale. While a material may appear perfectly homogeneous at one scale, it may be heterogeneous at another. A typical example for such a material is a composite, whose phases are distinguishable only at a small length scale and whose heterogeneous properties are linked to homogeneous properties at a larger scale. In general, the involved length scales are considered *separated* if their contrast is sufficiently high.[*] In such cases, it is reasonable to describe the homogenized behavior with classical, first-order theories. In contrast to that, when the scales are not clearly separated, the description of the homogenized behavior needs to be based on generalized, higher-order theories.

Generalized theories for materials are nowadays well-established. They trace back to the seminal work of Reference 2, who investigated the emergence and significance of couple stresses for the modeling of the size-dependent response of materials more than a hundred years ago. In their theory, the Cosserat brothers linked *couple stresses* to the gradient of a microscopic rotation field and classical *force stresses* to the gradient of the macroscopic translation field (i.e., the displacements). In that context, the microscopic rotation field is understood independent from the macroscopic rotation field. An extended theory based on the consideration of both macroscopic translational and macroscopic rotational degrees of freedom was later developed by the authors in References 3-5. We refer to References 6 and 7 for rigorous expositions of the Cosserats' couple-stress theory as well as to References 8-10 for further developments and generalizations.

Next to classical couple-stress theories, there exist a number of further approaches to the modeling of size effects in materials. An important branch is given by so-called *strain-gradient theories*, which for linear elastic solids have first been

---

proposed by Mindlin.[11] Associated theories are based on the incorporation of higher-order gradients of the displacement field into the material description. We refer to Reference 12 for further specifications based on the first gradient of strain and to Reference 13 for an extension involving the second gradient of strain. The interested reader is further referred to References 14 and 15 for underlying virtual-work and variational principles, respectively, to Reference 16 for extensions toward fully nonlinear settings, and to References 17-19 for possible numerical implementations. A general overview of gradient-extended continua is available through the monographs of References 20-22. Next to gradient-theories for elastic materials, there exists a rich theory on gradient-extended models for dissipative solids. In these cases, the gradient extensions are classically linked to internal variables like the plastic strains[23,24] and the damage field.[25] We refer to Reference 26 for associated variational treatments.

The above-mentioned formulations have in common that they incorporate the notion of microstructure (and its size) in a phenomenological way. In contrast to that, microstructural information about morphology and material properties can be accounted for in an explicit manner by means of *homogenization methods*. As in case of phenomenological material modeling, size effects may be incorporated in related schemes, depending on the existence of scale separation. If the considered scales are clearly separated, *classical* or *first-order* homogenization schemes are applicable; if they are not, *generalized* or *higher-order* schemes become necessary.

In the context of first-order homogenization schemes, we refer to References 27-31 for fundamental analytical approaches and to References 32-35 for seminal contributions to two-scale finite-element (FE) simulations. In the context of higher-order and generalized continua, analytical approaches have been explored by the authors in References 36-39, see also the overview by Forest[40] as well as the more recent contributions of References 41-45. Associated computational homogenization schemes have been developed in the framework of couple-stress and micromorphic theories by the authors in References 46-49 and in the framework of macroscopic strain-gradient approaches by the authors in References 50-53. We refer to References 54 and 55 for seminal treatments.

The present work is devoted to the *multiscale computational homogenization of gradient-extended continua* and unites ingredients of the works of[50] with respect to the gradient extensions at the homogenized scale, of[56] with regard to the algorithmic linearization of the macroscopic field equations, and of[57,58] with regard to spatial discretizations. In contrast to the contribution of,[50] which combines a Cauchy continuum at the lower length scale with a gradient-extended continuum at the larger length scale, we will take into account *gradient-extended continua at both scales*. This endeavor poses additional challenges not only for the theoretical treatment, but also for the numerical implementation.

From a theoretical perspective, we are dealing with overall three spatial scales given by (i) a *macroscopic scale*, at which the homogenized, gradient-extended behavior will be obtained through computational homogenization of (ii) a *mesoscopic scale*, at which we assume the presence of representative volume elements ($\mathcal{RVE}$), which are themselves characterized by size dependent material response at each mesoscopic material point and thus inherently linked to (iii) a *microscopic scale*, at which we assume the existence of a microstructure that we capture with phenomenological, gradient-extended material models. The latter could be motivated, for example, through the presence of microscopic fibers with spatial extensions and distributions that could still be distinguished from further morphological entities like holes, inclusions, and so forth at the level of the $\mathcal{RVE}$. We refer the interested reader to[59,60] for associated analytical, numerical and experimental details.

From a numerical perspective, challenges arise because the gradient extensions come along with the requirement of C^1-continuous approximations of independent fields at both scales. Such a requirement can be captured in an elegant way by employing *isogeometric analysis* (IGA) in the sense of References 57 and 58. A further algorithmic feature of the proposed implementation is due to the linearization of the macroscopic boundary value problem. Here, we employ the approach advocated by Miehe et al.,[56] which was originally developed in the context of first-order homogenization. As we will see, the associated gradient extensions result in settings that remind of the linearized structures appearing in the coupled homogenization schemes considered by the authors in References 61-63.

As the present work proposes a computational multiscale method based on numerical discretizations involving IGA at two scales, we denote it as IGA^2-method in analogy to the well-known FE^2-methods mentioned above. We refer to Reference 64 for a review of FE^2-methods and to Reference 65 for a general overview of computational multiscale techniques. As already mentioned, the motivation behind using IGA instead of classical finite elements is due to the straightforward and elegant implementation of C^1-continuous independent fields. In case of classical FE methods, the construction and implementation of higher-order element continuities is usually cumbersome. It could, for example, be realized by the use of Hermite shape functions, which however come with a complex algebraic structure and a high number of degrees of freedom, in particular in three spatial dimensions. Alternative FE approximations are given by mixed and nonconforming methods. While mixed methods can be implemented with standard C^0-type shape functions, they need to satisfy the

inf-sup condition.[66] Nonconforming finite elements indeed allow for a more or less straightforward numerical implementation at a reasonable amount of degrees of freedom,[67] still their finite-element function space is not a subspace of the solution space.[68] In contrast to that, IGA-based schemes do not suffer from such limitations, but allow for an elegant implementation of higher-order continuities.[†] As IGA-based multiscale methods have thus far been limited to homogeneous macroscopic problems,[73,74] we believe that the here proposed IGA²-method provides a useful and innovative framework for the modeling of higher-order continua across length scales.

The outline of the article is as follows. In Section 2, we discuss fundamental concepts of the multiscale modeling of higher-gradient continua. In that consequence, suitable boundary conditions based on an energetically consistent scale transition are derived. In Section 3, we discuss the numerical implementation of the proposed scheme. Here, we put an emphasis on the consistent linearization of the macroscopic field equations and the IGA-based discretization of representative volume elements (RVE). In Section 4, we present a number of benchmark tests to demonstrate the performance and accuracy of the proposed multiscale technique. We close the article with a summary and a conclusion in Section 5.

2 | PRELIMINARIES AND PROBLEM DESCRIPTION

In this section, we present the basic concepts for the homogenization of second- and third-gradient media for the macro- and microcontinuum. Moreover, suitable boundary conditions with respect to energetic criteria for the scale transition are provided. As higher-order tensor notations and operations on them are required, a brief summary is given in Appendix A.

2.1 | Macroscopic boundary value problem

We start with a short summary of the second-gradient macroscopic continuum. Therefore, we introduce a reference configuration $\overline{\Omega}_0 \subset \mathbb{R}^3$ with boundary $\partial\overline{\Omega}_0$ and outward unit normal $\overline{N}$ and a current configuration $\overline{\Omega} \subset \mathbb{R}^3$, with outward unit normal $\overline{n}$ and boundary $\partial\overline{\Omega}$, with subsets $\overline{\Gamma}^\varphi$ and $\overline{\Gamma}^\sigma$, and properties $\overline{\Gamma}^\varphi \cap \overline{\Gamma}^\sigma = \emptyset$ and $\overline{\Gamma}^\varphi \cup \overline{\Gamma}^\sigma = \delta\overline{\Omega}$. The deformation mapping $\overline{\varphi} : \overline{\Omega}_0 \to \mathbb{R}^3$ relates the reference and current configuration to each other, $\overline{\Omega} = \overline{\varphi}(\overline{\Omega}_0)$. Furthermore, the vector to an arbitrary material point P is labeled by $\overline{X} \in \overline{\Omega}_0$. In the current configuration, the location of the corresponding point p is given by $\overline{x} = \overline{\varphi}(\overline{X})$, see Figure 1.

The first-order deformation measure $\overline{F} : \overline{\Omega}_0 \to \mathbb{R}^{3\times3}$ and the second-order deformation measure $\overline{\mathfrak{F}} : \overline{\Omega}_0 \to \mathbb{R}^{3\times3\times3}$ are given by the first and second gradient of the mapping $\overline{\varphi}(\overline{X})$ as

$$\overline{F} = \overline{\nabla}\overline{\varphi} \quad \text{and} \quad \overline{\mathfrak{F}} = \overline{\nabla}^2\overline{\varphi}. \tag{1}$$
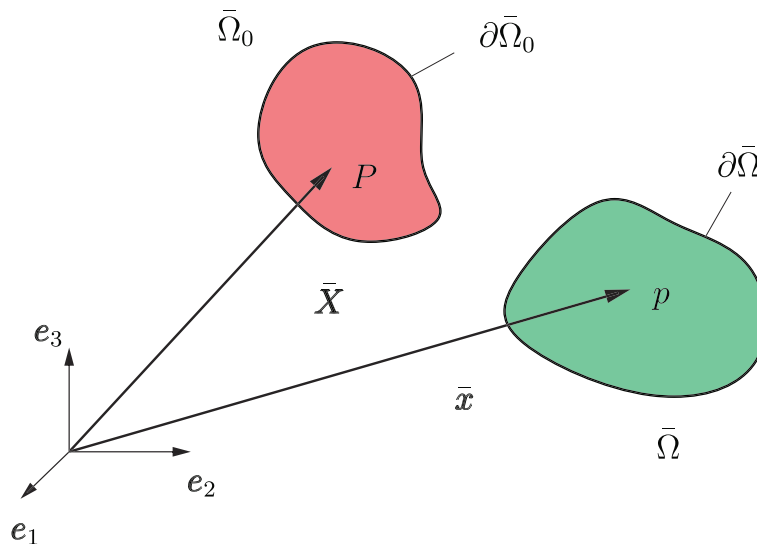

FIGURE 1   Reference and current configuration

Here, $\overline{\nabla}$ refers to the gradient with respect to $\overline{X}$, see (A3) in Appendix A. Following References 16, 75, and 76, we postulate the virtual work of the internal contributions as

$$\delta\overline{\Pi}^{\text{int}} = \int_{\overline{\Omega}_0} \left(\overline{P} : \delta\overline{F} + \overline{\mathfrak{P}} \ \vdots \ \delta\overline{\mathfrak{F}} \right) \ dV, \tag{2}$$

where $\overline{P}$ denotes the macroscopic two-point first Piola–Kirchhoff stress tensor and $\overline{\mathfrak{P}}$ the macroscopic two-point third-order stress tensor, conjugate to $\overline{\mathfrak{F}}$. Moreover,

$$\delta\overline{F} = \overline{\nabla}\delta\overline{\varphi} \quad \text{and} \quad \delta\overline{\mathfrak{F}} = \overline{\nabla}^2\delta\overline{\varphi}, \tag{3}$$

where the space of virtual or admissible test functions is given by

$$\mathcal{V} = \{\delta\overline{\varphi} \in \mathcal{H}^2(\overline{\Omega}) \mid \delta\overline{\varphi} = \mathbf{0}, \ \overline{\nabla}\delta\overline{\varphi}\,\overline{N} = \mathbf{0} \quad \text{on} \quad \overline{\Gamma}^{\varphi}\} \tag{4}$$

with boundary $\overline{\Gamma}^{\varphi}$, see Figure 2. Applying integration by parts twice in (2) yields

$$\delta\overline{\Pi}^{int}(\varphi) = \int_{\overline{\Omega}_0} \overline{\nabla} \cdot (\overline{\nabla} \cdot \overline{\mathfrak{P}} - \overline{P}) \cdot \delta\overline{\varphi}\,dV + \int_{\partial\overline{\Omega}_0} \delta\overline{\varphi} \cdot (\overline{P} - \overline{\nabla} \cdot \overline{\mathfrak{P}})\,\overline{N} + \overline{\nabla}\delta\overline{\varphi} : (\overline{\mathfrak{P}} \cdot \overline{N})dA. \tag{5}$$

Introducing the orthogonal decomposition $\overline{\nabla}_{\perp} \cdot (\bullet) = \overline{\nabla}(\bullet) : (\overline{N} \otimes \overline{N})$ and $\overline{\nabla}_{\parallel} \cdot (\bullet) = \overline{\nabla}(\bullet) : (I - \overline{N} \otimes \overline{N})$, we obtain after some further technical steps

$$\begin{aligned}
\delta\overline{\Pi}^{int}(\varphi) = &\int_{\overline{\Omega}_0} \overline{\nabla} \cdot (\overline{\nabla} \cdot \overline{\mathfrak{P}} - \overline{P}) \cdot \delta\overline{\varphi}\,dV + \int_{\partial\overline{\Omega}_0} \delta\overline{\varphi} \cdot (\overline{P} - \overline{\nabla} \cdot \overline{\mathfrak{P}})\,\overline{N}dA \\
&- \int_{\partial\overline{\Omega}_0} \left[\delta\overline{\varphi} \cdot (K\,(\overline{\mathfrak{P}}\,\overline{N})\,\overline{N} + \overline{\nabla}_{\parallel} \cdot (\overline{\mathfrak{P}}\,\overline{N})) - \overline{\nabla}_{\perp}\delta\overline{\varphi} : \left(\overline{\mathfrak{P}}\,\overline{N} \right) \right] dA \\
&+ \int_{\partial^2\overline{\Omega}_0} \delta\overline{\varphi} \cdot (\overline{\mathfrak{P}} : (\hat{\overline{N}} \otimes \overline{N}))dS,
\end{aligned} \tag{6}$$

for a sufficiently smooth $\overline{\Omega}_0$, where $\hat{\overline{N}}$ is the normal to $\partial^2\overline{\Omega}_0$ and the tangent to $\partial\overline{\Omega}_0$. Note that $\partial^2\overline{\Omega}_0$ is defined by the union of the boundary curves of the boundary surface patches and thus, $\hat{\overline{N}}$ can be defined differently from both adjacent surfaces, see Javili et al.[16] and the citations therein for details. Moreover, $K = -\overline{\nabla}_{\parallel} \cdot \overline{N}$ is the curvature of the surface.

Omitting line forces for the ease of exposition, the external contributions to the virtual work are given by

$$\delta\overline{\Pi}^{\text{ext}} = \int_{\overline{\Omega}_0} \overline{B}_{\text{ext}} \cdot \delta\overline{\varphi} \ dV + \int_{\overline{\Gamma}^{\sigma}} \overline{T}_{\text{ext}} \cdot \delta\overline{\varphi} \ dA + \int_{\overline{\Gamma}^{\nabla\sigma}} \overline{M}_{\text{ext}} : \overline{\nabla}_{\perp}\delta\overline{\varphi} \ dA \tag{7}$$

with the common body force per unit volume $\overline{B}_{\text{ext}}$, the traction forces $\overline{T}_{\text{ext}}$ on boundary $\overline{\Gamma}^{\sigma}$, and the hyperstress traction force $\overline{M}_{\text{ext}}$ on boundary $\overline{\Gamma}^{\nabla\sigma}$, see once again Figure 2.

Thus, the principle of virtual work reads

$$\delta\overline{\Pi}^{\text{int}} - \delta\overline{\Pi}^{\text{ext}} = 0 \ , \quad \forall \ \delta\overline{\varphi} \in \mathcal{V} \tag{8}$$

and the internal contributions can be related by applying partial integration and the Gaussian integral theorem to the external contributions, see Javili et al.:[16]

$$\overline{T}_{\text{ext}} = (\overline{P} - \overline{\nabla} \cdot \overline{\mathfrak{P}}) \, \overline{N},$$
$$\overline{M}_{\text{ext}} = \overline{\mathfrak{P}} \, \overline{N} \, . \tag{9}$$

Note, that the last equation can be decomposed in tangential and normal components, see Madeo et al.[77] for details. Taking the balance equation

$$\overline{\nabla} \cdot (\overline{P} - \overline{\nabla} \cdot \overline{\mathfrak{P}}) + \overline{B}_{\text{ext}} = \mathbf{0} \tag{10}$$

into account, completes the set of equations for the strong form of the second-gradient boundary value problem. In the following, we omit volumetric body forces as gravity forces, thereby $\overline{B}_{\text{ext}} = \mathbf{0}$.

2.2 | Mesoscopic boundary value problem

In every material point $\overline{P}$ of the macroscopic domain, we assume the existence of a representative volume element $\mathcal{RVE}$ on a mesoscale, sufficiently separated from the macroscale and sufficiently large to be *representative*, containing the information on the inhomogeneous mesoscopic continuum, see Figure 2. To be specific, we postulate a second-gradient material in the $\mathcal{RVE}$ analogous to (8) on the macroscale for two reasons: First, this general approach for the homogenization from a second-gradient micro-continuum toward a second-gradient macro-continuum allows us to demonstrate that the formulation proposed by Kouznetsova et al.[50] is a special case of the methodology presented next. Second, we can now generalize this concept for general higher-order materials.

We start with the mapping for the microscopic relative position of the material points $x = \varphi(X)$:

$$\varphi(X) = \overline{F} \, X + \frac{1}{2} \, \overline{\overline{\mathfrak{F}}} \, : \, (X \otimes X) + \tilde{w}. \tag{11}$$

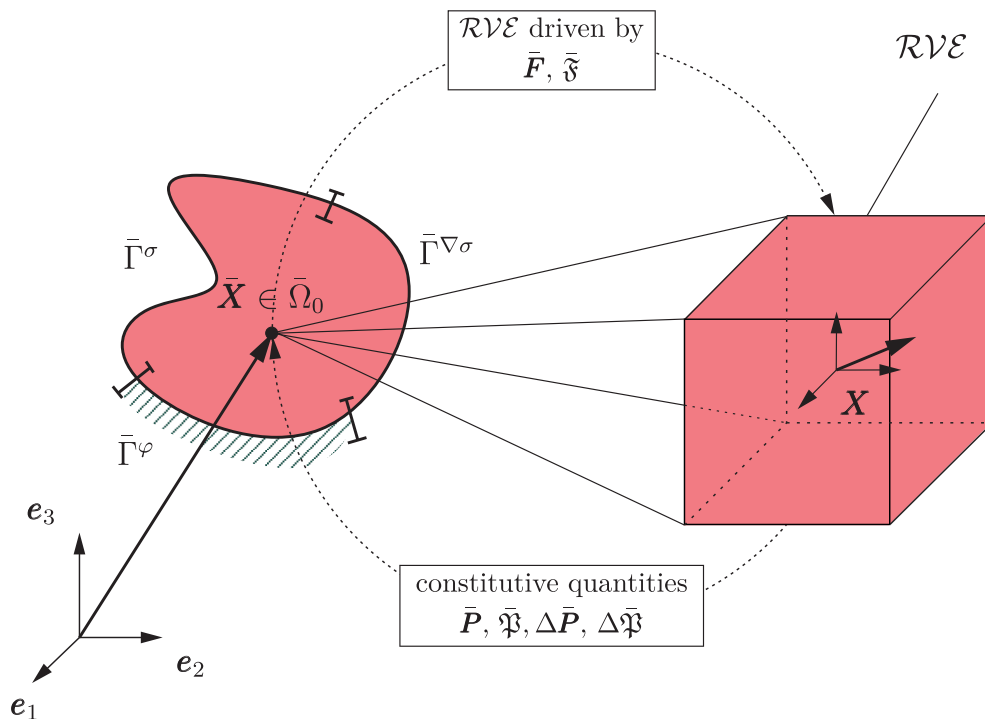

FIGURE 2 Meso-macro transition of the mechanical boundary value problem, left: boundary decomposition of the macroscopic continuum in Dirichlet boundaries $\overline{\Gamma}^{\varphi}$ and Neumann boundaries $\overline{\Gamma}^{\sigma}, \overline{\Gamma}^{\nabla \sigma}$ of the traction force and the hyperstress traction force, right: $\mathcal{RVE}$ as defined for every macroscopic point

Here, $\tilde{w}$ describes the unknown microcroscopic fluctuation field, which includes all higher-order terms of the Taylor series expansion, see Kouznetsova et al..[50] In analogy to the macroscopic quantities, we obtain the microscopic first-order deformation measure $\boldsymbol{F} = \nabla\boldsymbol{\varphi}$ and the second-order deformation measure $\mathfrak{F} = \nabla^2\boldsymbol{\varphi}$:

$$\boldsymbol{F} = \overline{\boldsymbol{F}} + \overline{\mathfrak{F}}\,\boldsymbol{X} + \tilde{\boldsymbol{F}} \quad \text{and} \quad \mathfrak{F} = \overline{\mathfrak{F}} + \tilde{\mathfrak{F}}, \tag{12}$$

where $\tilde{\boldsymbol{F}} := \nabla\tilde{w}$ and $\tilde{\mathfrak{F}} := \nabla^2\tilde{w}$. The averaged microscopic deformations over the volume of the $\mathcal{RVE}$ can be connected to the macroscopic counterparts $\overline{\boldsymbol{F}}$ and $\overline{\mathfrak{F}}$ via

$$\frac{1}{V}\int_{\mathcal{RVE}} \boldsymbol{F}\,\mathrm{d}V = \overline{\boldsymbol{F}} \quad \text{and} \quad \frac{1}{V}\int_{\mathcal{RVE}} \mathfrak{F}\,\mathrm{d}V = \overline{\mathfrak{F}}, \tag{13}$$

see Appendix B[‡] for further information. The local balance equation of the microscopic second-gradient continuum is given analogously to (10) by:

$$\nabla \cdot \left[\boldsymbol{P} - \nabla \cdot \mathfrak{P}\right] = \boldsymbol{0}, \tag{14}$$

where $\boldsymbol{P} := \partial_F \Psi(\boldsymbol{F}, \mathfrak{F})$ and $\mathfrak{P} := \partial_{\mathfrak{F}} \Psi(\boldsymbol{F}, \mathfrak{F})$ are defined in terms of a Helmholtz energy function Ψ.

The macro-homogeneity condition is given by an energetic criterion that states that the virtual work applied to the system in the material point $\overline{P}$ is equal to the virtual work in the $\mathcal{RVE}$, hence we assume

$$\frac{1}{V}\int_{\mathcal{RVE}} \left(\boldsymbol{P} : \nabla\delta\boldsymbol{\varphi} + \mathfrak{P} \;\vdots\; \nabla^2\delta\boldsymbol{\varphi}\right)\mathrm{d}V = \overline{\boldsymbol{P}} : \delta\overline{\boldsymbol{F}} + \overline{\mathfrak{P}} \;\vdots\; \delta\overline{\mathfrak{F}}. \tag{15}$$

Note that this excludes Neumann conditions on the $\mathcal{RVE}$, which would add an effective contribution to the virtual work on the mesoscale. The left-hand side of the energetic criterion can be rewritten as

$$\frac{1}{V}\int_{\mathcal{RVE}} \boldsymbol{P}\,\mathrm{d}V : \delta\overline{\boldsymbol{F}} + \frac{1}{V}\int_{\mathcal{RVE}} (\boldsymbol{P} \otimes \boldsymbol{X} + \mathfrak{P})\,\mathrm{d}V \;\vdots\; \delta\overline{\mathfrak{F}} = \overline{\boldsymbol{P}} : \delta\overline{\boldsymbol{F}} + \overline{\mathfrak{P}} \;\vdots\; \delta\overline{\mathfrak{F}}, \tag{16}$$

see Appendix C. Comparing the left- and right-hand sides of the last equation, yields

$$\overline{\boldsymbol{P}} = \frac{1}{V}\int_{\mathcal{RVE}} \boldsymbol{P}\,\mathrm{d}V \quad \text{and} \quad \overline{\mathfrak{P}} = \underbrace{\frac{1}{V}\int_{\mathcal{RVE}} \boldsymbol{P} \otimes \boldsymbol{X}\,\mathrm{d}V}_{\overline{\mathfrak{P}}^{P}} + \underbrace{\frac{1}{V}\int_{\mathcal{RVE}} \mathfrak{P}\,\mathrm{d}V}_{\overline{\mathfrak{P}}^{\mathfrak{P}}}. \tag{17}$$

Here, the macroscopic third-order stress tensor $\overline{\mathfrak{P}}$ is split into $\overline{\mathfrak{P}}^{P}$, which is given by the volume average of the first moment of the microscopic stresses $\boldsymbol{P}$, and $\overline{\mathfrak{P}}^{\mathfrak{P}}$, which is a volume average of the microscopic third-order stress tensor $\mathfrak{P}$. Note that if a first-gradient material within the $\mathcal{RVE}$ is assumed, the macroscopic hyperstress $\overline{\mathfrak{P}}^{\mathfrak{P}}$ vanishes and we obtain the formulation provided by Kouznetsova et al..[50] To obtain information about the boundary conditions, (15) can be rewritten as:

$$\frac{1}{V}\int_{\mathcal{RVE}} \left(\left[\overline{\boldsymbol{P}} - \boldsymbol{P}\right] : [\delta\overline{\boldsymbol{F}} + \delta\overline{\mathfrak{F}}\,\boldsymbol{X} - \delta\boldsymbol{F}] + \left[\overline{\mathfrak{P}}^{\mathfrak{P}} - \mathfrak{P}\right] \;\vdots\; \left[\delta\overline{\mathfrak{F}} - \delta\mathfrak{F}\right]\right)\mathrm{d}V = 0, \tag{18}$$

see Appendix D.1. Obviously, the simplest assumption for all points of the mesoscale, that fulfills the last equation is given by postulating the constraints $\overline{\boldsymbol{P}} := \boldsymbol{P}$ or $\delta\overline{\boldsymbol{F}} + \delta\overline{\mathfrak{F}}\,\boldsymbol{X} := \delta\boldsymbol{F}$ and additionally $\overline{\mathfrak{P}}^{\mathfrak{P}} := \mathfrak{P}$ or $\delta\overline{\mathfrak{F}} := \delta\mathfrak{F}$, compare Schröder[64] in the context of first-order theories. An alternative expression of (18) yields:

$$\frac{1}{V} \int\limits_{\partial \mathcal{RVE}} \left(\left[\overline{\mathfrak{P}}^{\mathfrak{P}} - \mathfrak{P} \right] \boldsymbol{N} \right) : \left[\delta \overline{\boldsymbol{F}} + \delta \overline{\mathfrak{F}} \, \boldsymbol{X} - \delta \boldsymbol{F} \right] \, \mathrm{d}A$$

$$+ \frac{1}{V} \int\limits_{\partial \mathcal{RVE}} \left(\left[\overline{\boldsymbol{P}} - (\boldsymbol{P} - \nabla \cdot \mathfrak{P}) \right] \boldsymbol{N} \right) \cdot \left[\delta \overline{\boldsymbol{F}} \, \boldsymbol{X} + \frac{1}{2} \delta \overline{\mathfrak{F}} : (\boldsymbol{X} \otimes \boldsymbol{X}) - \delta \boldsymbol{\varphi} \right] \, \mathrm{d}A = 0, \tag{19}$$

see Appendix D.2 for further information. Thus, regarding a deformation-driven approach, suitable Dirichlet boundary conditions on the boundary $\partial \mathcal{RVE}$ are

$$\overline{\boldsymbol{F}} \, \boldsymbol{X} + \frac{1}{2} \overline{\mathfrak{F}} : (\boldsymbol{X} \otimes \boldsymbol{X}) - \boldsymbol{\varphi} = \boldsymbol{0},$$

$$\overline{\boldsymbol{F}} + \overline{\mathfrak{F}} \, \boldsymbol{X} - \boldsymbol{F} = \boldsymbol{0}, \tag{20}$$

satisfying (19). Note that due to $\overline{\mathfrak{F}}$ the boundaries are quadratic functions.

For a stress driven approach, (19) yields possible Neumann boundary conditions, however, that would render an inherently complex implementation for large deformations, see Kouznetsova.[75] A comparison of the Dirichlet boundary conditions with the mappings (11) and (12)$_1$ provides the following relationship for these conditions, $\tilde{\boldsymbol{w}} = \boldsymbol{0}$ and $\nabla \tilde{\boldsymbol{w}} = \boldsymbol{0}$ on the boundary. Furthermore, the microscopic stress tractions are $\boldsymbol{T}_{\text{ext}} = (\boldsymbol{P} - \nabla \cdot \mathfrak{P}) \, \boldsymbol{N}$ and the hyperstress tractions are given by $\boldsymbol{M}_{\text{ext}} = \mathfrak{P} \, \boldsymbol{N}$, periodic boundary conditions as shown in Figure 3 require

$$\tilde{\boldsymbol{w}}(\boldsymbol{X}^+) = \tilde{\boldsymbol{w}}(\boldsymbol{X}^-) \,, \qquad \boldsymbol{T}_{\text{ext}}(\boldsymbol{X}^+) = -\boldsymbol{T}_{\text{ext}}(\boldsymbol{X}^-),$$

$$\nabla \tilde{\boldsymbol{w}}(\boldsymbol{X}^+) = \nabla \tilde{\boldsymbol{w}}(\boldsymbol{X}^-) \,, \qquad \boldsymbol{M}_{\text{ext}}(\boldsymbol{X}^+) = -\boldsymbol{M}_{\text{ext}}(\boldsymbol{X}^-), \tag{21}$$

satisfying the energetic criterion (15). Here, $\boldsymbol{X}^+$ and $\boldsymbol{X}^-$ refer to opposite surfaces, see Figure 3 for details. Note, that the tangential part of the constraint $\nabla \tilde{\boldsymbol{w}} = \boldsymbol{0}$ is already fulfilled by the condition $\tilde{\boldsymbol{w}} = \boldsymbol{0}$. Therefore, we can either restrict the gradient term to the normal component or, alternatively, make use of a least-square minimization approach within the context of Mortar domain decomposition methods. We refer to Reference 78 for details on the theoretical background and to References 79 and 80 for the implementation.

Note that the periodicity is given in terms of the fluctuation $\tilde{\boldsymbol{w}}$, that is, with regard to (11) follows immediately that the geometrical boundaries for a second-order problem are not periodic within the $\mathcal{RVE}$ in contrast to a first-order problem. To be specific, the boundary deformation emanating from $\overline{\boldsymbol{F}}$ is periodic whereas the deformation emanating from $\overline{\mathfrak{F}}$ is not due to the quadratic formulation in $\boldsymbol{X}$. The latter term does not drop out if (21), left, is formulated in the total deformation $\boldsymbol{\varphi}(\boldsymbol{X})$.
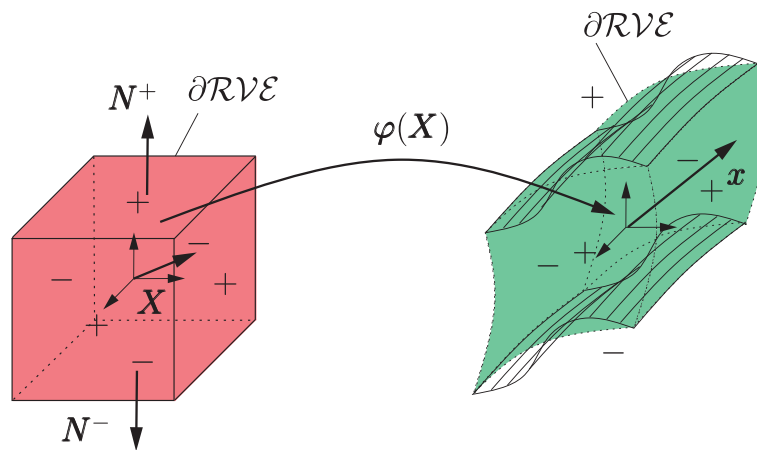

FIGURE 3 Mesoscopic boundary value problem, periodic boundary conditions on $\partial \mathcal{RVE}$, here only displayed for top and bottom for better understanding

Remark 1. Third-gradient medium: The proposed formulation at hand can be extended in a straightforward manner toward a macroscopic third-gradient medium with hyperstress $\overline{\mathbb{P}}$ and the conjugate deformation measure $\overline{\mathbb{F}} = \overline{\nabla}^3 \overline{\boldsymbol{\varphi}}$. The corresponding application of the energetic criterion reads

$$\frac{1}{V} \int\limits_{\mathcal{RVE}} \left(\boldsymbol{P} : \nabla \delta \boldsymbol{\varphi} + \mathfrak{P} \;\vdots\; \nabla^2 \delta \boldsymbol{\varphi} \right) \, \mathrm{d}V = \overline{\boldsymbol{P}} : \delta \overline{\boldsymbol{F}} + \overline{\mathfrak{P}} \;\vdots\; \delta \overline{\mathfrak{F}} + \overline{\mathbb{P}} :: \delta \overline{\mathbb{F}}. \tag{22}$$

The mapping of the microscopic position reads

$$\boldsymbol{\varphi}(\boldsymbol{X}) = \overline{\boldsymbol{F}} \boldsymbol{X} + \frac{1}{2} \overline{\mathfrak{F}} : (\boldsymbol{X} \otimes \boldsymbol{X}) + \frac{1}{6} \overline{\mathbb{F}} \;\vdots\; (\boldsymbol{X} \otimes \boldsymbol{X} \otimes \boldsymbol{X}) + \tilde{\boldsymbol{w}}. \tag{23}$$

Insertion yields the relations

$$\begin{aligned}
\overline{\boldsymbol{P}} &= \frac{1}{V} \int\limits_{\mathcal{RVE}} \boldsymbol{P} \, \mathrm{d}V, \\
\overline{\mathfrak{P}} &= \underbrace{\frac{1}{V} \int\limits_{\mathcal{RVE}} \boldsymbol{P} \otimes \boldsymbol{X} \, \mathrm{d}V}_{\overline{\mathfrak{P}}^P} + \underbrace{\frac{1}{V} \int\limits_{\mathcal{RVE}} \mathfrak{P} \, \mathrm{d}V}_{\overline{\mathfrak{P}}^{\mathfrak{P}}}, \\
\overline{\mathbb{P}} &= \underbrace{\frac{1}{V} \int\limits_{\mathcal{RVE}} \frac{1}{2} \boldsymbol{P} \otimes \boldsymbol{X} \otimes \boldsymbol{X} \, \mathrm{d}V}_{\overline{\mathbb{P}}^P} + \underbrace{\frac{1}{V} \int\limits_{\mathcal{RVE}} \mathfrak{P} \otimes \boldsymbol{X} \, \mathrm{d}V}_{\overline{\mathbb{P}}^{\mathfrak{P}}},
\end{aligned} \tag{24}$$

where we have again made use of $\int_{\mathcal{RVE}} \boldsymbol{X} \mathrm{d}V = \boldsymbol{0}$, see Appendices B–D. This yields the set of Dirichlet boundary conditions

$$\begin{aligned}
\overline{\boldsymbol{F}} \boldsymbol{X} + \frac{1}{2} \overline{\mathfrak{F}} : (\boldsymbol{X} \otimes \boldsymbol{X}) + \frac{1}{6} \overline{\mathbb{F}} \;\vdots\; (\boldsymbol{X} \otimes \boldsymbol{X} \otimes \boldsymbol{X}) - \boldsymbol{\varphi} &= \boldsymbol{0}, \\
\overline{\boldsymbol{F}} + \overline{\mathfrak{F}} \boldsymbol{X} + \frac{1}{2} \overline{\mathbb{F}} : (\boldsymbol{X} \otimes \boldsymbol{X}) - \boldsymbol{F} &= \boldsymbol{0},
\end{aligned} \tag{25}$$

where we omit again further discussion on possible (periodic) Neumann conditions. With this at hand, a first-gradient medium within the $\mathcal{RVE}$ can be established by removing all terms related to $\mathfrak{P}$. An extension toward a third-gradient medium within the $\mathcal{RVE}$ seems plausible, but up to now constitutive equations for this need further investigations. Moreover, we note here, that a typical $\mathcal{RVE}$ is in the range of μm, and thus, inhomogeneities in the first Piola–Kirchhoff stress tensor are weighted with μm² in $\overline{\mathbb{P}}$, which is often negligible and the reason, why we do not further take this into account here. For further information on scale separation, see Schröder.[64]

3 | CONSISTENT LINEARIZATION AND DISCRETIZATION

For the computation of the macroscopic boundary value problem with attached mesoscopic $\mathcal{RVE}$s, we introduce here the IGA²-method, analogous to the FE²-method, see Schröder[64] and references therein. We omit here details on the spline-based discretization of the macroscale within the concept of IGA, as numerous papers have already presented this and instead focus on the mesoscopic $\mathcal{RVE}$, assuming that the discrete macroscopic quantities of the deformations $(\overline{\boldsymbol{F}}, \overline{\mathfrak{F}})$ are known at the particular Newton step. Note that higher-order continua at the macroscale require appropriate continuity of the spline based discretization.

Thus, in a first step the macroscopic quantities $(\overline{\boldsymbol{F}}, \overline{\mathfrak{F}})$ are transferred to the mesoscale $\mathcal{RVE}$ at every material point, see Figure 2. After that, the boundary value problem on the mesoscale is solved using suitable boundary conditions and the homogenization is performed using volumetric averaged mesoscopic quantities as well as the linearization of these quantities. In the last step, the macroscopic boundary value problem is solved and the next Newton iteration starts.

3.1 | Linearization of macroscopic stresses and hyperstresses

Since the macroscopic boundary value problem is solved with a Newton–Raphson iteration, we need a consistent linearization of the macroscopic field equations. Therefore, it is necessary to linearize the stresses $\overline{\boldsymbol{P}}$ and $\overline{\mathfrak{P}}$, evaluated via the incremental relations:

$$\Delta\overline{\boldsymbol{P}} := \frac{\partial\overline{\boldsymbol{P}}}{\partial\overline{\boldsymbol{F}}} : \Delta\overline{\boldsymbol{F}} + \frac{\partial\overline{\boldsymbol{P}}}{\partial\overline{\mathfrak{F}}} \;\vdots\; \Delta\overline{\mathfrak{F}} \quad\text{and}\quad \Delta\overline{\mathfrak{P}} := \frac{\partial\overline{\mathfrak{P}}}{\partial\overline{\boldsymbol{F}}} : \Delta\overline{\boldsymbol{F}} + \frac{\partial\overline{\mathfrak{P}}}{\partial\overline{\mathfrak{F}}} \;\vdots\; \Delta\overline{\mathfrak{F}}. \tag{26}$$

However, the macroscopic quantities are given by the averaged mesoscopic stresses and hyperstresses, hence $\overline{\boldsymbol{P}} := \overline{\boldsymbol{P}}(\boldsymbol{P}(\boldsymbol{F}, \mathfrak{F}))$ and $\overline{\mathfrak{P}} := \overline{\mathfrak{P}}(\boldsymbol{P}(\boldsymbol{F}, \mathfrak{F}), \mathfrak{P}(\boldsymbol{F}, \mathfrak{F}))$, see (17). Thus we have to use the chain rule for the partial derivative of the macroscopic stresses with respect to the corresponding deformations and end up after some calculations with:

$$\begin{aligned}\left[\Delta\overline{\boldsymbol{P}}\right]_{iJ} = {} & \frac{1}{V}\int_{\mathcal{RVE}} [\mathbb{C}]_{iJsT}\ \mathrm{d}V\ \left[\Delta\overline{\boldsymbol{F}}\right]_{sT} \\ & + \frac{1}{V}\int_{\mathcal{RVE}} \left([\mathbb{C}]_{iJsT}\ [\boldsymbol{X}]_U + [\mathsf{D}]_{iJsTU}\right)\mathrm{d}V\ \left[\Delta\overline{\mathfrak{F}}\right]_{sTU} \\ & + \frac{1}{V}\int_{\mathcal{RVE}} \left([\mathbb{C}]_{iJsT}\ \left[\Delta\tilde{\boldsymbol{F}}\right]_{sT} + [\mathsf{D}]_{iJsTU}\ \left[\Delta\tilde{\mathfrak{F}}\right]_{sTU}\right)\mathrm{d}V\end{aligned} \tag{27}$$

and

$$\begin{aligned}\left[\Delta\overline{\mathfrak{P}}\right]_{iJK} = {} & \frac{1}{V}\int_{\mathcal{RVE}} \left([\mathbb{C}]_{iJsT}\ [\boldsymbol{X}]_K + [\mathsf{E}]_{iJKsT}\right)\ \mathrm{d}V\ \left[\Delta\overline{\boldsymbol{F}}\right]_{sT} \\ & + \frac{1}{V}\int_{\mathcal{RVE}} \big([\mathbb{C}]_{iJsT}\ [\boldsymbol{X}]_K\ [\boldsymbol{X}]_U + [\mathsf{D}]_{iJsTU}\ [\boldsymbol{X}]_K \\ & \qquad\qquad + [\mathsf{E}]_{iJKsT}\ [\boldsymbol{X}]_U + [\mathsf{G}]_{iJKsTU}\big)\mathrm{d}V\ \left[\Delta\overline{\mathfrak{F}}\right]_{sTU} \\ & + \frac{1}{V}\int_{\mathcal{RVE}} \left([\mathbb{C}]_{iJsT}\ [\boldsymbol{X}]_K + [\mathsf{E}]_{iJKsT}\right)\ \left[\Delta\tilde{\boldsymbol{F}}\right]_{sT}\ \mathrm{d}V \\ & + \frac{1}{V}\int_{\mathcal{RVE}} \left([\mathsf{D}]_{iJsTU}\ [\boldsymbol{X}]_K + [\mathsf{G}]_{iJKsTU}\right)\ \left[\Delta\tilde{\mathfrak{F}}\right]_{sTU}\mathrm{d}V,\end{aligned} \tag{28}$$

where the derivatives of the stresses are defined by:

$$\mathbb{C} := \frac{\partial\boldsymbol{P}}{\partial\boldsymbol{F}}, \quad \mathsf{D} := \frac{\partial\boldsymbol{P}}{\partial\mathfrak{F}}, \quad \mathsf{E} := \frac{\partial\mathfrak{P}}{\partial\boldsymbol{F}}, \quad\text{and}\quad \mathsf{G} := \frac{\partial\mathfrak{P}}{\partial\mathfrak{F}}, \tag{29}$$

see Appendix E for more details. It is obvious, that the linearizations of the macroscopic stresses $\overline{\boldsymbol{P}}$ and $\overline{\mathfrak{P}}$ depend on the sensitivity of the mesoscopic fluctuations $\Delta\tilde{\boldsymbol{F}}$ and $\Delta\tilde{\mathfrak{F}}$, defined in (12). The correlation between these sensitivities and the change of the corresponding macroscopic fields $\Delta\overline{\boldsymbol{F}}$ and $\Delta\overline{\mathfrak{F}}$ can be done in the discrete setting by linearization of the virtual work of the mesoscopic boundary value problem in the solution point, as shown next.

3.2 | Linearization of mesoscopic boundary value problem

The relationship between these sensitivities and the macroscopic fields follows from the mesoscopic boundary value problem. With regard to (14) and assuming that $\delta\tilde{\boldsymbol{w}} = \boldsymbol{0}$ holds on the whole boundary, we obtain

$$G := \int_{\mathcal{RVE}} \left(\boldsymbol{P} : \delta\tilde{\boldsymbol{F}} + \mathfrak{P} \;\vdots\; \delta\tilde{\mathfrak{F}}\right)\ \mathrm{d}V. \tag{30}$$

Solving the problem such that $G = 0$, it follows immediately that $\Delta G = 0$. Hence, the linearization in the equilibrium state reads

$$\Delta G := \int_{\mathcal{RVE}} \left(\delta \tilde{\boldsymbol{F}} : \left[\mathbb{C} : \Delta \boldsymbol{F} + \mathsf{D} \vdots \Delta \mathfrak{F} \right] + \delta \tilde{\mathfrak{F}} \vdots \left[\mathsf{E} : \Delta \boldsymbol{F} + \mathsf{G} \vdots \Delta \mathfrak{F} \right] \right) \, \mathrm{d}V = 0, \tag{31}$$

where

$$\Delta \boldsymbol{F} = \Delta \overline{\boldsymbol{F}} + \Delta \overline{\mathfrak{F}} \, \boldsymbol{X} + \Delta \tilde{\boldsymbol{F}} \quad \text{and} \quad \Delta \mathfrak{F} = \Delta \overline{\mathfrak{F}} + \Delta \tilde{\mathfrak{F}}. \tag{32}$$

This can be evaluated in the discrete setting, as will be shown next.

3.3 | Mesoscopic finite element approximation

Next, we have to approximate the fluctuation field, the virtual and the incremental fluctuation fields:

$$\tilde{\boldsymbol{w}}^{\mathrm{h}} = \sum_{A \in \mathcal{I}} R^A \, \tilde{\boldsymbol{q}}^A, \quad \delta \tilde{\boldsymbol{w}}^{\mathrm{h}} = \sum_{A \in \mathcal{I}} R^A \, \delta \tilde{\boldsymbol{q}}^A, \quad \text{and} \quad \Delta \tilde{\boldsymbol{w}}^{\mathrm{h}} = \sum_{A \in \mathcal{I}} R^A \, \Delta \tilde{\boldsymbol{q}}^A, \tag{33}$$

where $R^A : \mathcal{RVE} \to \mathbb{R}$ are B-spline[§] based shape functions of order p with associated control points $A \in \mathcal{I} = 1, \dots, m$ with the overall number of control points m. Furthermore, $\left[\tilde{\boldsymbol{q}}^A, \delta \tilde{\boldsymbol{q}}^A, \Delta \tilde{\boldsymbol{q}}^A \right] \in \mathbb{R}^3$. So, the deformation tensors lead to the approximation

$$\tilde{\boldsymbol{F}}^{\mathrm{h}} = \sum_{A \in \mathcal{I}} \tilde{\boldsymbol{q}}^A \otimes \nabla R^A \quad \text{and} \quad \tilde{\mathfrak{F}}^{\mathrm{h}} = \sum_{A \in \mathcal{I}} \tilde{\boldsymbol{q}}^A \otimes \nabla^2 R^A, \tag{34}$$

which are given analogously for the virtual ($\delta \tilde{\boldsymbol{F}}^{\mathrm{h}}$, $\delta \tilde{\mathfrak{F}}^{\mathrm{h}}$) and the incremental ($\Delta \tilde{\boldsymbol{F}}^{\mathrm{h}}$, $\Delta \tilde{\mathfrak{F}}^{\mathrm{h}}$) deformation tensors. Note that we can also discretize the displacement field $\boldsymbol{\varphi}(\boldsymbol{X})$ using (11) as well.

For the boundary conditions, we first introduce Dirichlet conditions as presented in (20). For the implementation of a first-order mesoscale continuum is straightforward, as we only have to deal with linear conditions in $\boldsymbol{X}$. Using open knot vectors, which are interpolatory at the boundaries, the control points of the spline has to be distributed linearly along the boundaries of the $\mathcal{RVE}$. For higher-order problems, we obtain quadratic (second-order formulations) and cubic (third-order formulations) boundaries in $\boldsymbol{X}$. Therefore, we make use of a least-square optimization for the ease of implementation. However, the problem itself can be solved exactly, that is, quadratic or higher order splines can reproduce a quadratic boundary, compare Reference 81. Introducing a set of evaluation points $\hat{\boldsymbol{q}}_i$ along the boundary and a set of control points $\tilde{\boldsymbol{q}}_j$ for the splines-based discretization of the discrete boundary $\partial \mathcal{RVE}^{\mathrm{h}}$, the least-square problem reads

$$\{ \tilde{\boldsymbol{q}}_j \} = \underbrace{\min}_{\tilde{\boldsymbol{q}}_i \in \partial \mathcal{RVE}^{\mathrm{h}}} \| \hat{\boldsymbol{q}}_i - \sum_j R^j(\boldsymbol{\xi}_i) \, \tilde{\boldsymbol{q}}^j \|. \tag{35}$$

Note, that $\hat{\boldsymbol{q}}_i = \overline{\boldsymbol{F}} \, \boldsymbol{q}_i + \frac{1}{2} \, \overline{\mathfrak{F}} : (\boldsymbol{q}_i \otimes \boldsymbol{q}_i)$ and $\nabla \hat{\boldsymbol{q}}_i = \overline{\boldsymbol{F}} + \overline{\mathfrak{F}} \, \boldsymbol{q}_i$, with the position of the evaluation point in the reference configuration $\boldsymbol{q}_i$. We refer to the textbook[81] and the discussion therein on the enforcement of Dirichlet conditions for further information on the evaluation of the least-square problem. For second-order boundaries, the least-square problem is expanded by the constraint $\nabla \tilde{\boldsymbol{w}}(\boldsymbol{X}) = \boldsymbol{0}$ on all surfaces to

$$\{ \tilde{\boldsymbol{q}}_j \} = \underbrace{\min}_{\tilde{\boldsymbol{q}}_i \in \partial \mathcal{RVE}^{\mathrm{h}}} \left\| \begin{matrix} \hat{\boldsymbol{q}}_i - \sum_j R^j(\boldsymbol{\xi}_i) \, \tilde{\boldsymbol{q}}^j \\ \nabla \hat{\boldsymbol{q}}_i - \sum_j \nabla R^j(\boldsymbol{\xi}_i) \, \tilde{\boldsymbol{q}}^j \end{matrix} \right\|. \tag{36}$$

For periodic boundary conditions, we have to ensure that (21), left, is valid. For general higher-order domain decomposition problems using nonconforming meshes, we refer to our previous developments in References 79 and 80, applied

here on conforming meshes. For the ease of implementation, we note that a least-square optimization using

$$
\{\tilde{\boldsymbol{q}}_j^-\} = \underbrace{\min}_{\tilde{\boldsymbol{q}}_i^- \in \partial \mathcal{RVE}^h} \left\| \begin{array}{c} \sum_k R^k(\boldsymbol{\xi}_i^+)\,\tilde{\boldsymbol{q}}^k - \sum_j R^j(\boldsymbol{\xi}_i^-)\,\tilde{\boldsymbol{q}}^j + \left(\hat{\boldsymbol{q}}_i^+ - \hat{\boldsymbol{q}}_i^-\right) \\ \sum_k \nabla R^k(\boldsymbol{\xi}_i^+)\,\tilde{\boldsymbol{q}}^k - \sum_j \nabla R^j(\boldsymbol{\xi}_i^-)\,\tilde{\boldsymbol{q}}^j + \left(\nabla \hat{\boldsymbol{q}}_i^+ - \nabla \hat{\boldsymbol{q}}_i^-\right) \end{array} \right\|, \tag{37}
$$

can also be applied, leaving a nodal dependency in the form $\tilde{\boldsymbol{q}}_j^- := \tilde{\boldsymbol{q}}_j^-(\tilde{\boldsymbol{q}}_j^+)$ for the set of opposing evaluation points $\{\boldsymbol{q}_i^+, \boldsymbol{q}_i^-\}$.

Next, we can establish a relationship between the mesoscopic sensitivities and the change of corresponding macroscopic fields. For this, we discretize the last two sections in reverse order and insert the approximations in a first step in the equilibrium state of the mesoscopic boundary value problem (31)

$$
\begin{aligned}
\Delta G^h := & \int_{\mathcal{RVE}^h} \delta \tilde{\boldsymbol{F}}^h : \left[\mathbb{C}^h : \left(\Delta \overline{\boldsymbol{F}} + \Delta \overline{\mathfrak{F}}\, \boldsymbol{X}^h + \Delta \tilde{\boldsymbol{F}}^h \right) + \mathsf{D}^h : \left(\Delta \overline{\mathfrak{F}} + \Delta \tilde{\mathfrak{F}}^h \right) \right]\, \mathrm{d}V \\
& + \int_{\mathcal{RVE}^h} \delta \tilde{\mathfrak{F}}^h : \left[\mathsf{E}^h : \left(\Delta \overline{\boldsymbol{F}} + \Delta \overline{\mathfrak{F}}\, \boldsymbol{X}^h + \Delta \tilde{\boldsymbol{F}}^h \right) + \mathsf{G}^h : \left(\Delta \overline{\mathfrak{F}} + \Delta \tilde{\mathfrak{F}}^h \right) \right]\, \mathrm{d}V = 0,
\end{aligned} \tag{38}
$$

where the discrete derivatives of the stresses are defined by

$$
\mathbb{C}^h := \mathbb{C}\left(\boldsymbol{F}^h, \mathfrak{F}^h\right),\ \mathsf{D}^h := \mathsf{D}\left(\boldsymbol{F}^h, \mathfrak{F}^h\right),\ \mathsf{E}^h := \mathsf{E}\left(\boldsymbol{F}^h, \mathfrak{F}^h\right),\ \text{and}\ \mathsf{G}^h := \mathsf{G}\left(\boldsymbol{F}^h, \mathfrak{F}^h\right). \tag{39}
$$

After some calculations, see Appendix F for further information, we arrive at the discrete correlation between the mesoscopic sensitivities and the change of corresponding macroscopic fields:

$$
\left[\Delta \tilde{\boldsymbol{q}}\right]_s^B = -\left([\boldsymbol{K}]_{ls}^{AB}\right)^{-1} \left([\mathfrak{L}]_{lrT}^A \left[\Delta \overline{\boldsymbol{F}}\right]_{rT} + [\mathbb{M}]_{lrTU}^A \left[\Delta \overline{\mathfrak{F}}\right]_{rTU} \right). \tag{40}
$$

Here, $\boldsymbol{K}$, $\mathfrak{L}$, and $\mathbb{M}$ are the stiffness matrices of the mesoscopic boundary value problem.

In a second step, we discretize the macroscopic stresses (27) and (28), where we use the correlation of the mesoscopic sensitivities to the macroscopic quantities (40) and end up in:

$$
\begin{aligned}
\left[\Delta \overline{\boldsymbol{P}}\right]_{iJ}^h = & \left\{ \left[\mathbb{V}^{\mathbb{C}}\right]_{iJrT}^h - \left[\mathfrak{N}\right]_{iJs}^B \left([\boldsymbol{K}]_{ls}^{AB}\right)^{-1} [\mathfrak{L}]_{lrT}^A \right\} \left[\Delta \overline{\boldsymbol{F}}\right]_{rT} \\
& + \left\{ \left[\mathsf{V}^{\mathbb{CD}}\right]_{iJrTU}^h - \left[\mathfrak{N}\right]_{iJs}^B \left([\boldsymbol{K}]_{ls}^{AB}\right)^{-1} [\mathbb{M}]_{lrTU}^A \right\} \left[\Delta \overline{\mathfrak{F}}\right]_{rTU},
\end{aligned} \tag{41}
$$

for the linearization of the stresses and:

$$
\begin{aligned}
\left[\Delta \overline{\mathfrak{P}}\right]_{iJK}^h = & \left\{ \left[\mathsf{V}^{\mathbb{CE}}\right]_{iJKrT}^h - \left[\mathbb{N}\right]_{iJKs}^B \left([\boldsymbol{K}]_{ls}^{AB}\right)^{-1} [\mathfrak{L}]_{lrT}^A \right\} \left[\Delta \overline{\boldsymbol{F}}\right]_{rT} \\
& + \left\{ \left[\mathsf{V}^{\mathbb{CDEG}}\right]_{iJKrTU}^h - \left[\mathbb{N}\right]_{iJKs}^B \left([\boldsymbol{K}]_{ls}^{AB}\right)^{-1} [\mathbb{M}]_{lrTU}^A \right\} \left[\Delta \overline{\mathfrak{F}}\right]_{rTU},
\end{aligned} \tag{42}
$$

for the linearization of the hyperstresses, see Appendix G for further information on the volume averaged tensors $\mathbb{V}^{\mathbb{C}}$, $\mathsf{V}^{\mathbb{CD}}$, $\mathsf{V}^{\mathbb{CE}}$, and $\mathsf{V}^{\mathbb{CDEG}}$ as well as $\mathfrak{N}$ and $\mathbb{N}$. This description of the linearization of the macroscopic stresses and hyperstresses is free of the mesoscopic fluctuations $\tilde{\boldsymbol{w}}$ and the discretized version $\tilde{\boldsymbol{q}}^A$, respectively.

4 | NUMERICAL EXPERIMENTS

In this section, we investigate the performance and accuracy of the homogenization technique for different materials. We start with some benchmark tests for a Mooney–Rivlin material and a second-gradient material for fiber-reinforced polymers for the $\mathcal{RVE}$. Afterwards, we use this second-gradient material for investigations using the well-known Cook's membrane.

4.1 | Benchmark test: Mooney–Rivlin material

As a first proof of concept, we investigate $\mathcal{RVE}$ using a homogeneous Mooney–Rivlin material, see Reference 60. The edge length of the $\mathcal{RVE}$ cube is 0.1 mm and the coordinate system is fixed in the center of the cube, see Figure 4.

The first-order constitutive relation is given by

$$\Psi(J, I_1, I_2) = c (J - 1)^2 - d \ln(J) + c_1 (I_1 - 3) + c_2 (I_2 - 3). \tag{43}$$

Here, $J = \det(\mathbf{F})$, $I_1 = \text{tr}(\mathbf{F}^{\text{T}} \mathbf{F}) = \mathbf{F} : \mathbf{F}$, and $I_2 = \text{tr}(\text{cof}(\mathbf{F}^{\text{T}} \mathbf{F}))$. Moreover, $c = 1/3 (c_1 + c_2)$, $d = 2 (c_1 + 2 c_2)$, $c_1 = 2000$ MPa, and $c_2 = 1000$ MPa. To test the $\mathcal{RVE}$, we define the macroscopic deformation tensor:

$$\overline{\mathbf{F}} := \begin{bmatrix} 0.897 & 0.500 & -0.400 \\ -0.070 & 1.001 & -0.100 \\ 0.082 & 0.020 & 0.997 \end{bmatrix}, \tag{44}$$

and assume the macroscopic second gradient to be $\overline{\mathfrak{F}} := \langle$. With this information, we solve the microscopic boundary value problem, where we apply in a first step Dirichlet boundaries on $\partial \mathcal{RVE}$ and in a second step periodic boundaries, see Figure 4 for details.

In Figure 5, the von Mises stresses are plotted for the $\mathcal{RVE}$ with Dirichlet and periodic boundary conditions. In particular, we increase the number of elements in each direction of the cube from 4, 8 to 16 elements using B-splines of order $p = 2$. Since the Mooney–Rivlin material is of first order with linear constraints on the boundary, we obtain a homogeneous distribution of the stress field.

Since we use an energetic criterion within the homogenization, we compare the maximum error $E_{\max}(\Psi)$ of the (analytically evaluated) strain energy $\Psi_{\text{ana}} := \Psi(\overline{\mathbf{F}})$ with the averaged strain energy $\overline{\Psi}_{\mathcal{RVE}} := \frac{1}{V} \int_{\mathcal{RVE}} \Psi(\mathbf{F}^{\text{h}}) dV$ of the $\mathcal{RVE}$, see Table 1. In particular, we make use of the following error definitions for the relative maximal error $E_{\max}$ and the relative error of the norm E_{norm}

$$E_{\max}(\bullet) = \frac{\max(\text{abs}((\bullet)_{\text{ana}} - (\bullet)_{\mathcal{RVE}}))}{||(\bullet)_{\text{ana}}||} , \quad E_{\text{norm}}(\bullet) = \frac{||(\bullet)_{\text{ana}} - (\bullet)_{\mathcal{RVE}}||}{||(\bullet)_{\text{ana}}||}. \tag{45}$$

Moreover, we make use of the same error definition for the stresses $\partial_{\mathbf{F}} \Psi(\overline{\mathbf{F}})$ and for the tangent $\partial_{\mathbf{F}}^2 \Psi(\overline{\mathbf{F}})$. Note that the relative maximum errors $E_{\max}(\bullet)$ and the relative errors in the norm $E_{\text{norm}}(\bullet)$ for the energy, stresses and tangent are in the range of 1.48E − 16 to 1.27E − 14.

4.2 | Benchmark test: Second-gradient material

In this second example, we apply the proposed concept for second-order gradient materials. In Reference 59, the whole deformation has been prescribed such that a constant curvature generates a homogeneous hyperstress field. Here, we
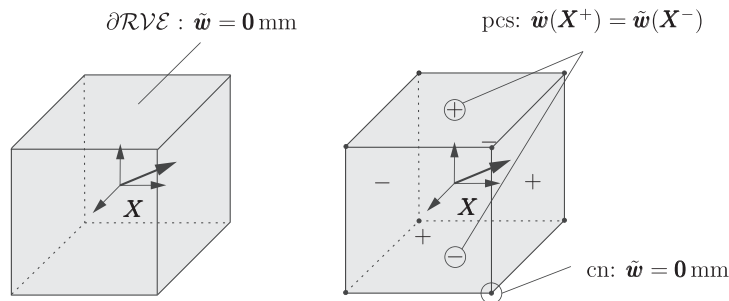

FIGURE 4 Mooney–Rivlin material. Left: $\mathcal{RVE}$ (edge length 0.1 mm) with Dirichlet boundaries $\tilde{\mathbf{w}} = \mathbf{0}$ mm on $\partial \mathcal{RVE}$. Right: $\mathcal{RVE}$ with periodic boundary conditions $\tilde{\mathbf{w}}(\mathbf{X}^+) = \tilde{\mathbf{w}}(\mathbf{X}^-)$ for the periodically contiguous surfaces (pcs) top-bottom, right-left, front-back, and eight constrained corner nodes (cn) with $\tilde{\mathbf{w}} = \mathbf{0}$ mm
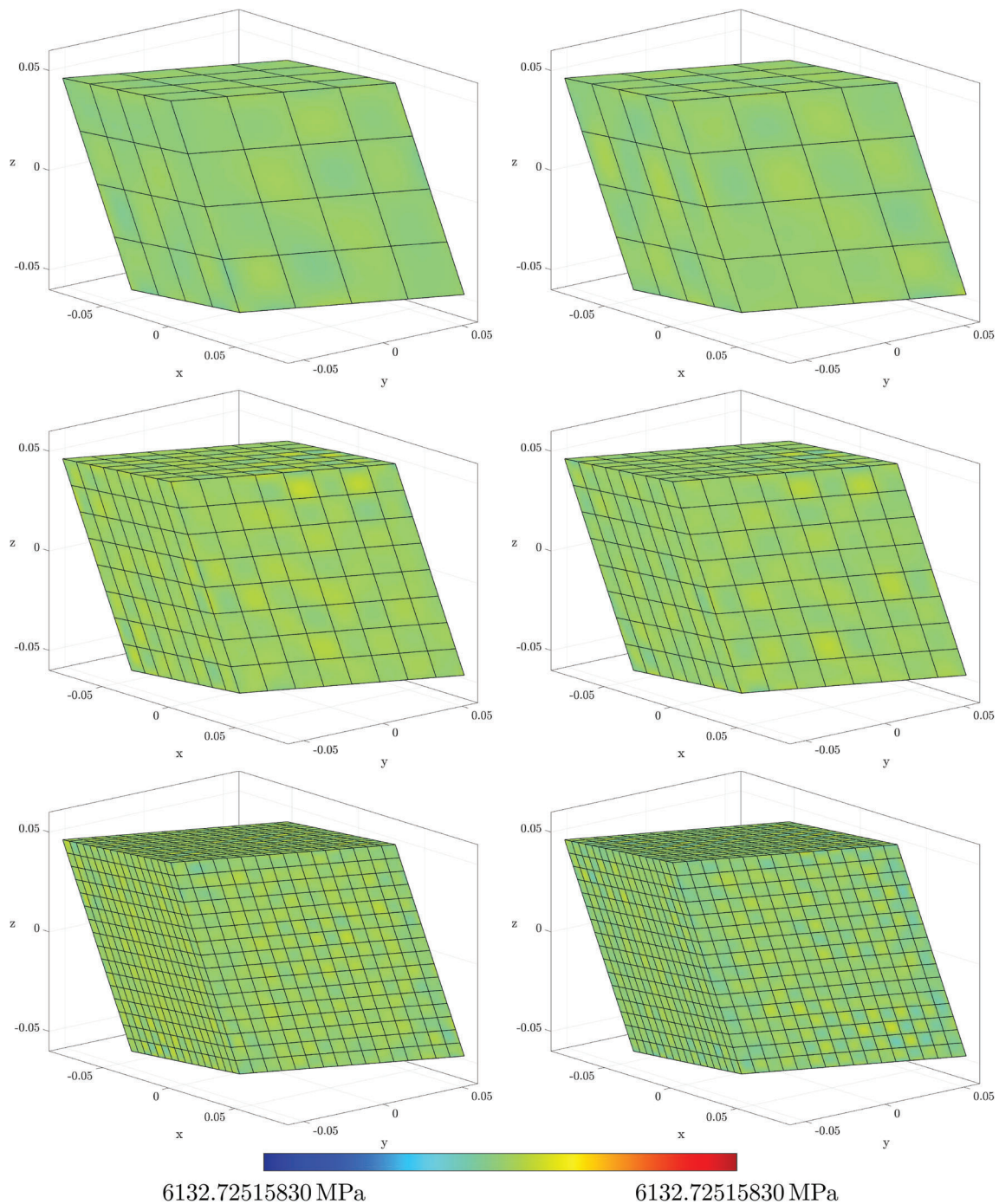
FIGURE 5 Mooney–Rivlin material. Von Mises stresses—Left to right: $\mathcal{RVE}$ with Dirichlet and periodic boundaries, top to bottom: 4, 8, and 16 elements in each direction

prescribe again the boundary of the RVE and evaluate the balance equations to obtain the aimed hyperstress field. To be precise, we make use of fiber-reinforced polymers (frp) as proposed in References 76 and 82 with a composed stored energy function of the form

$$\Psi_{\text{frp}} := \zeta\, \Psi_{\text{mat}} + \frac{1-\zeta}{2}\, \Psi_{\text{fib}}, \tag{46}$$

where $\zeta \in [0, 1]$ is the volume fraction of the matrix material. Ψ_{mat} denotes the stored energy function of the matrix material and Ψ_{fib} denotes the stored energy function of the fibers, both given as follows

TABLE 1 Mooney–Rivlin material

Elements	$4 \times 4 \times 4$		$8 \times 8 \times 8$		$16 \times 16 \times 16$	
Boundary	**Dirichlet**	**Periodic**	**Dirichlet**	**Periodic**	**Dirichlet**	**Periodic**
$E_{\max}(\overline{\Psi})$	6.18E − 16	3.71E − 16	1.00E − 16	1.00E − 16	8.29E − 15	8.29E − 15
$E_{\max}(\overline{P})$	3.38E − 16	2.24E − 16	1.43E − 15	1.43E − 15	7.65E − 15	7.65E − 15
$E_{\mathrm{norm}}(\overline{P})$	5.03E − 16	3.49E − 16	1.62E − 15	1.62E − 15	1.19E − 14	7.65E − 15
$E_{\max}(\partial_{\overline{F}}\overline{P})$	2.23E − 16	1.48E − 16	4.45E − 16	4.45E − 16	4.68E − 15	4.68E − 15
$E_{\mathrm{norm}}(\partial_{\overline{F}}\overline{P})$	4.36E − 16	4.00E − 16	1.27E − 15	1.26E − 15	1.27E − 14	1.27E − 14

Note: Relative maximum error of the energies $E_{\max}(\overline{\Psi})$ (1st row). Relative maximum error $E_{\max}(\bullet)$ and relative error in the norm $E_{\mathrm{norm}}(\bullet)$ for the stresses and tangent (2nd–5th row). Here, for 4, 8, and 16 elements in each direction and the Dirichlet and periodic boundaries, respectively.

TABLE 2 Second-gradient material

Parameter of matrix material	c_1	2000	MPa
Parameter of matrix material	c_2	1000	MPa
Volume fraction of matrix material	ζ	0.5	–
Shear parameter of fiber material	a_{F}	15,000	MPa
Stretch parameter of fiber material	b_{F}	3000	MPa
Curvature parameter of fiber material	c_{F}	1.25	N
Orientation of fiber 1	$\boldsymbol{L}^1$	$\frac{1}{\sqrt{4.25}}[-1; -1; 1.5]$	–
Orientation of fiber 2	$\boldsymbol{L}^2$	$\frac{1}{\sqrt{4.25}}[-1; -1; -1.5]$	–
Initial angle of fibers	β	$\mathrm{acos}\left(\boldsymbol{L}^1 \cdot \boldsymbol{L}^2\right)$	rad

Note: Material setting of the fiber-reinforced polymer.

$$\Psi_{\mathrm{mat}} := \Psi(J, I_1, I_2),$$
$$\Psi_{\mathrm{fib}} := a_{\mathrm{F}} \tan^2\varphi + \frac{1}{2} \sum_\alpha \left[b_{\mathrm{F}} (\lambda^\alpha - 1)^2 + c_{\mathrm{F}}\, \boldsymbol{\kappa}^\alpha \cdot \left(\boldsymbol{F}\,\boldsymbol{F}^{\mathrm{T}}\, \boldsymbol{\kappa}^\alpha \right) \right], \tag{47}$$

where we make use of the Mooney–Rivlin material given in (43) for the matrix material Ψ_{mat}. The stiffness parameter a, b and c are related to the shear, stretch and curvature of the fiber material (Table 2).

Using bidirectional fibers with $\alpha = [1, 2]$, for the normalized fiber orientation $\boldsymbol{L}^\alpha$ in the reference configuration and the initial angle β between both directions, the spatial field of the fiber directions reads $\boldsymbol{l}^\alpha = \boldsymbol{F}\,\boldsymbol{L}^\alpha$. The stretch of the fibers λ^α can now be expressed as

$$\lambda^\alpha = ||\boldsymbol{l}^\alpha|| = ||\boldsymbol{F}\,\boldsymbol{L}^\alpha||, \tag{48}$$

whereas the spatial angle reads

$$\varphi = \mathrm{acos}\left(\tilde{\boldsymbol{l}}^1 \cdot \tilde{\boldsymbol{l}}^2 \right) - \beta. \tag{49}$$

Hence, we can write for the deformed fiber configuration $\boldsymbol{l}^\alpha = \lambda^\alpha\, \tilde{\boldsymbol{l}}^\alpha$. The curvature measure for the fiber initially aligned in $\boldsymbol{L}^\alpha$-direction is introduced as follows

$$\boldsymbol{\kappa}^\alpha = \frac{1}{(\lambda^\alpha)^2} \left(\boldsymbol{I} - \tilde{\boldsymbol{l}}^\alpha \otimes \tilde{\boldsymbol{l}}^\alpha \right) \mathfrak{F} : \left(\boldsymbol{L}^\alpha \otimes \boldsymbol{L}^\alpha \right). \tag{50}$$
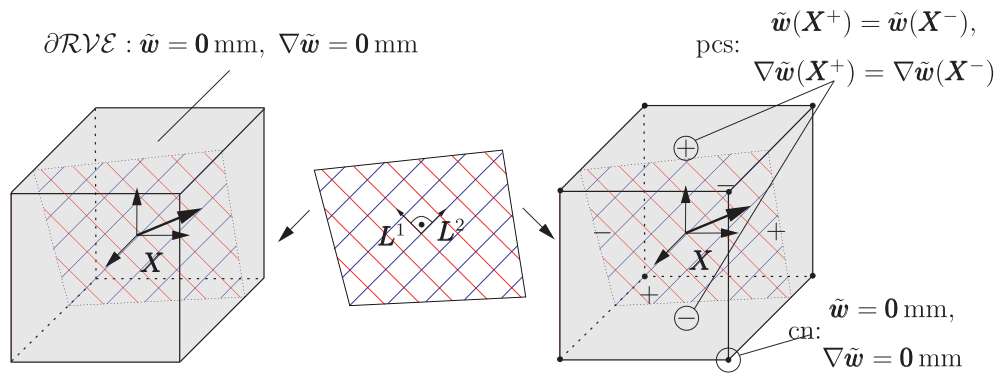
FIGURE 6 Homogeneous second-gradient material. Left: $\mathcal{RVE}$ in the reference configuration with edge length 0.1 mm and Dirichlet boundaries on $\partial\mathcal{RVE}$. Middle: Schematic representation of the long fibers in the polymer with direction $\boldsymbol{L}^\alpha$. Right: $\mathcal{RVE}$ with periodic boundary conditions, for the periodically contiguous surfaces (pcs) top-bottom, right-left, front-back, and constrained corner nodes (cn)

The macroscopic values of $\overline{\boldsymbol{F}}$ and $\overline{\mathfrak{F}}$ are again predefined

$$\overline{\boldsymbol{F}} := \begin{bmatrix} 0.897 & 0.500 & -0.400 \\ -0.400 & 1.001 & -0.100 \\ 0.082 & 0.020 & 0.997 \end{bmatrix}, \quad \overline{\mathfrak{F}}(1,:) := \begin{bmatrix} -0.033 & 0.015 & -0.020 \\ 0.015 & 0.013 & 0.043 \\ -0.020 & 0.043 & 0.029 \end{bmatrix},$$

$$\overline{\mathfrak{F}}(2,:) := \begin{bmatrix} 0.015 & -0.005 & 0.024 \\ -0.005 & 0.028 & 0.028 \\ 0.024 & 0.028 & 0.014 \end{bmatrix}, \quad \overline{\mathfrak{F}}(3,:) := \begin{bmatrix} 0.023 & 0.005 & -0.031 \\ 0.005 & -0.042 & -0.001 \\ -0.031 & -0.001 & -0.012 \end{bmatrix}.$$

(51)

In a first step, Dirichlet boundaries are applied on the boundary $\partial\mathcal{RVE}$, see Figure 6, left. Therefore, the boundaries are deformed satisfying the quadratic configuration provided in (20), constraining $\tilde{\boldsymbol{w}} = \boldsymbol{0}$ and $\nabla\tilde{\boldsymbol{w}} = \boldsymbol{0}$.

In a second step, we have applied periodic boundaries on $\partial\mathcal{RVE}$, requiring a higher-order coupling of all opposing surfaces. Moreover, the predefined macroscopic deformation due to $\overline{\boldsymbol{F}}$ and $\overline{\mathfrak{F}}$ has to be satisfied on all eight corner nodes, see Figure 6. The edge length of the $\mathcal{RVE}$ cube is $l = 0.1$ mm and the coordinate system is placed in the center of the cube, see Figure 6.

In Figure 7, the von Mises stress and the norm of the second-order stress $\mathfrak{P}$ are plotted for 16 elements in every direction. Again, we compare the solution of the constitutive relation at the mesoscale as defined in (47) with the analytical solution of (47) applied on the macroscale, see Table 3 for additional details. It can be seen, that the two shown ways of the enforcement of the energetic criterion result in different stress distributions, especially regarding the second-order contributions.

In addition, to demonstrate the accuracy of the formulation, we aim at a pure second-gradient material. Since this anisotropic second-gradient contribution is not well defined (it is singular without first-gradient contributions), we have to stabilize the formulation using small first-gradient contributions. To be specific, we reduced the constitutive parameters successively up to a factor of 1E − 08. In each direction 16 elements using quadratic B-splines ($p = 2$) for the analysis have been applied with Dirichlet boundaries, see (20). The maximum absolute error of the averaged values of $\boldsymbol{F}^{\mathrm{h}}$, $\mathfrak{F}^{\mathrm{h}}$, and $\mathfrak{P}^{\mathrm{h}}$ for a second-gradient material is shown with regard to the (analytically evaluated) values on the macroscale. The remaining error $E_{\max}(\mathfrak{P}^{\mathrm{h}})$ depends directly on the remaining first-gradient stiffness contributions. Thus, the second-gradient contributions converge to the correct analytical value as expected for a second-gradient material for a constant $\mathfrak{F}^{\mathrm{h}}$ deformation, as shown in Table 3.

4.3 | Second-gradient material with inclusions

Next, the previously introduced second-gradient material is applied on a geometrically inhomogeneous $\mathcal{RVE}$ with a 3D cross inclusion in the center. These types of inhomogeneities are used, for example, to reduce weight in 3D printed materials. In this example, we consider the inclusions as a void by setting the material parameters to approximately
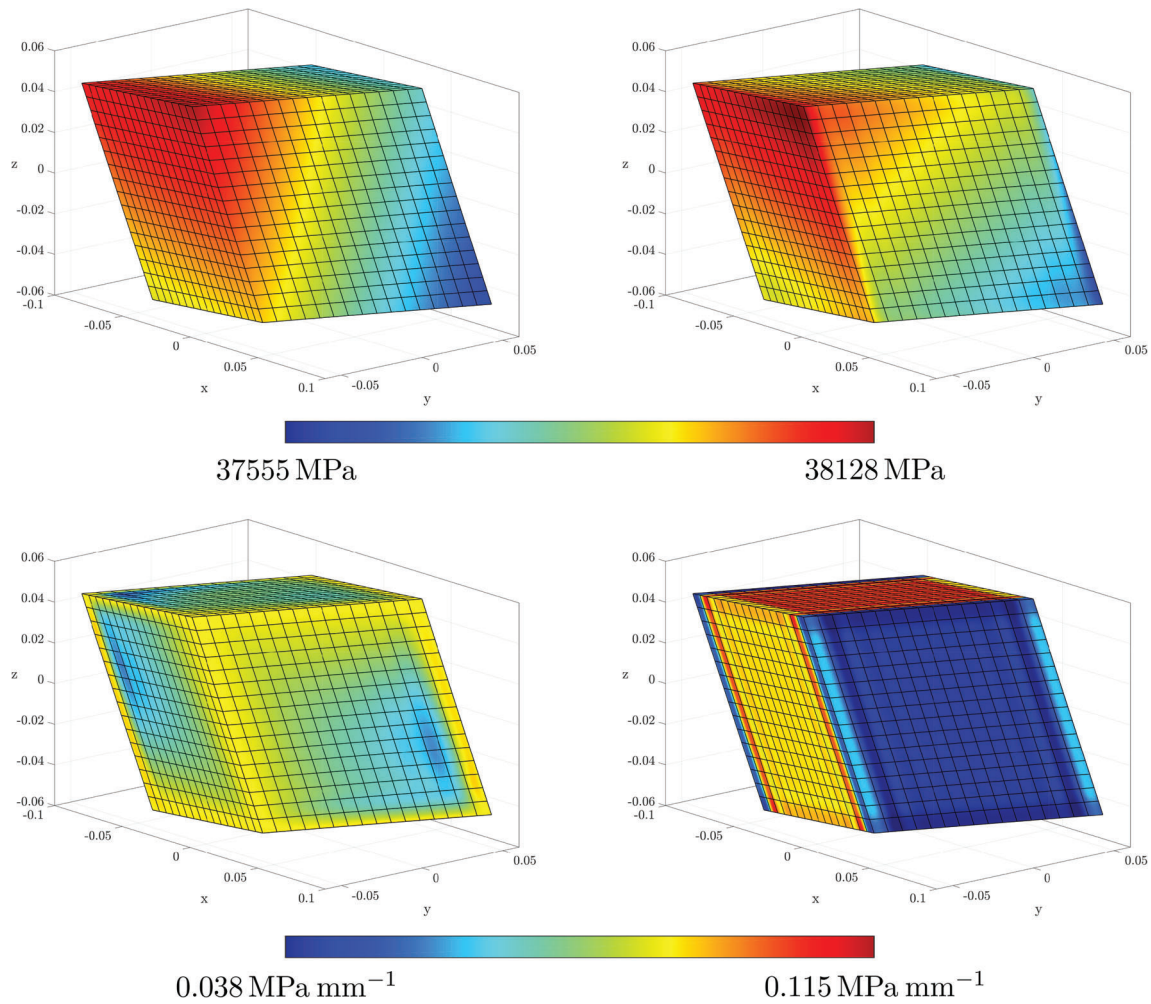
FIGURE 7 Homogeneous second-gradient material. Stresses for $\mathcal{RVE}$ with 16 elements in each direction—Left to right: Dirichlet and periodic boundaries, top to bottom: von Mises stress and $||\mathfrak{P}||$

TABLE 3 Homogeneous second-gradient material

Scaling	1E − 0	1E − 2	1E − 4	1E − 6	1E − 8
$E_{\max}(\boldsymbol{F}^{\mathrm{h}})$	1.58E − 14	1.57E − 14	1.59E − 14	1.59E − 14	1.56E − 14
$E_{\max}(\mathfrak{F}^{\mathrm{h}})$	4.59E − 13	4.59E − 13	4.60E − 13	4.60E − 13	4.59E − 13
$E_{\max}(\mathfrak{P}^{\mathrm{h}})$	1.74E + 01	1.81E − 01	1.80E − 03	2.58E − 05	1.84E − 05
$||\overline{\mathfrak{P}}^{P}||/||\overline{\overline{\mathfrak{P}}}||$	100%	21.6%	0.23%	0.00367%	0.00217%

Note: Relative absolute maximum error of $\boldsymbol{F}^{\mathrm{h}}$, $\mathfrak{F}^{\mathrm{h}}$, and $\mathfrak{P}^{\mathrm{h}}$ along with the norm of $\overline{\mathfrak{P}}^{P}$ in relation to the total norm of $\overline{\overline{\mathfrak{P}}}$ for a second-gradient material with minimal first-gradient contributions, scaled by the parameter as given in the row "scaling."

zero.[¶] Again, Dirichlet and periodic boundary conditions are applied, see Figure 8. The edge length of the $\mathcal{RVE}$ cube is again $l = 0.1$ mm with the coordinate system placed in the center. The 3D cross consists of two different edge lengths. The short edges are of the length $l/6$ and the long edges are of the length $l/4$, see Figure 8 for details.

In Figure 9, the von Mises stresses of the matrix and the fibers are plotted, cutting the $\mathcal{RVE}$ in half. Here, 24 quadratic B-splines elements in each direction of the $\mathcal{RVE}$ are used. Note that we observe the expected anisotropic stress distribution.
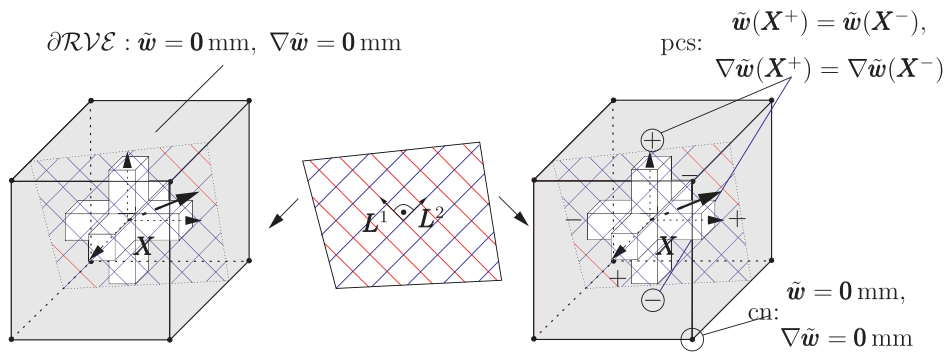
FIGURE 8 Second-gradient material with a void. Left: $\mathcal{RVE}$ (edge length 0.1 mm) with a 3D cross void and Dirichlet boundaries on $\partial\mathcal{RVE}$, see (20), middle: schematic representation of the long fibers in the polymer with direction $\boldsymbol{L}^\alpha$, right: $\mathcal{RVE}$ with a 3D cross void and periodic boundary conditions, see (21), for the periodically contiguous surfaces (pcs) top-bottom, right-left, front-back except the eight corner nodes (cn), where Dirichlet boundaries are used, see (20)
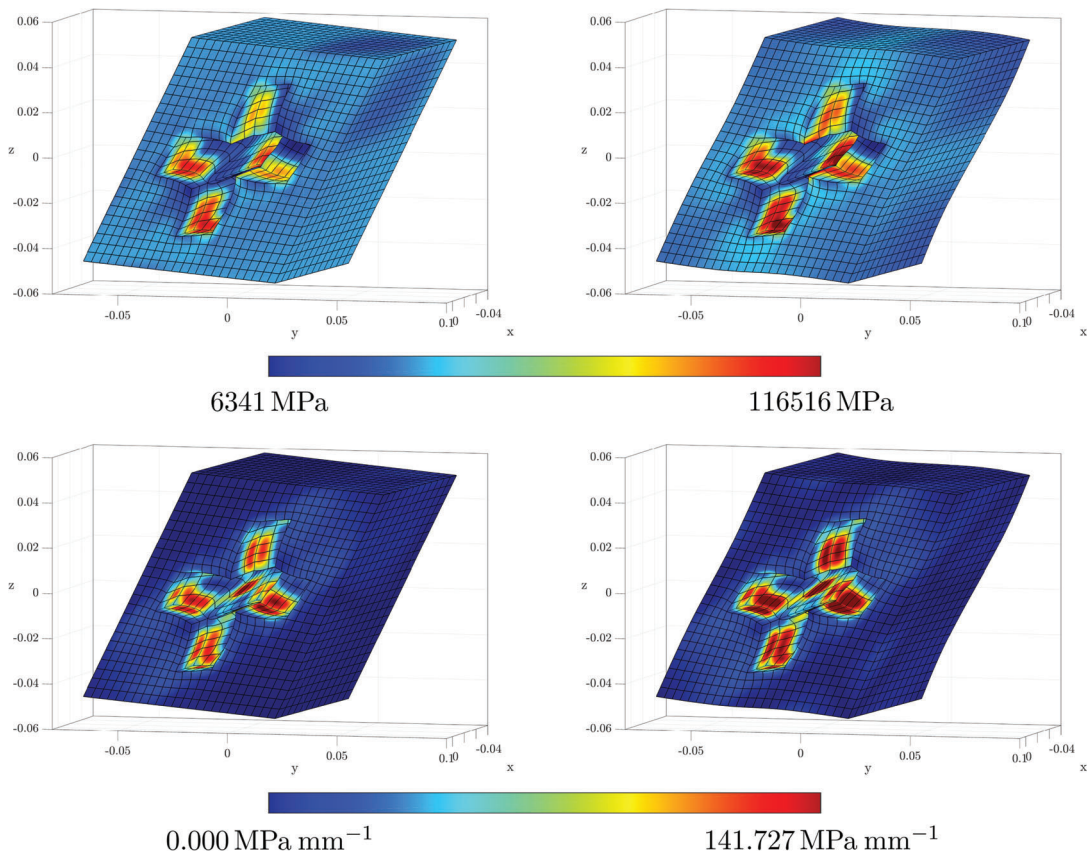
FIGURE 9 Second-gradient material with a void. Von Mises stresses for a half $\mathcal{RVE}$ with 24 elements in each direction—left to right: Dirichlet and periodic boundaries, top to bottom: von Mises stress and $||\boldsymbol{\mathfrak{B}}||$. Note that elements within the void are excluded from the plot

4.4 | Cook's membrane

In a last example, we examine a Cook's membrane as macroscopic system, see Figure 10, left, using again the second-gradient model for the microscopic system inheriting a void as described in Section 4.3. All other parameters are given in Table 2.

For the macroscopic system, the Cook's membrane is clamped on the left side, that is, $\overline{\boldsymbol{\varphi}} = \boldsymbol{0}$ mm on $\overline{\Gamma}^\varphi$. On the right-hand side of the Cook's membrane, a constant traction force $\overline{\boldsymbol{T}}_{ext} = [0;\ 100;\ 0]$ N is applied. We use quadratic
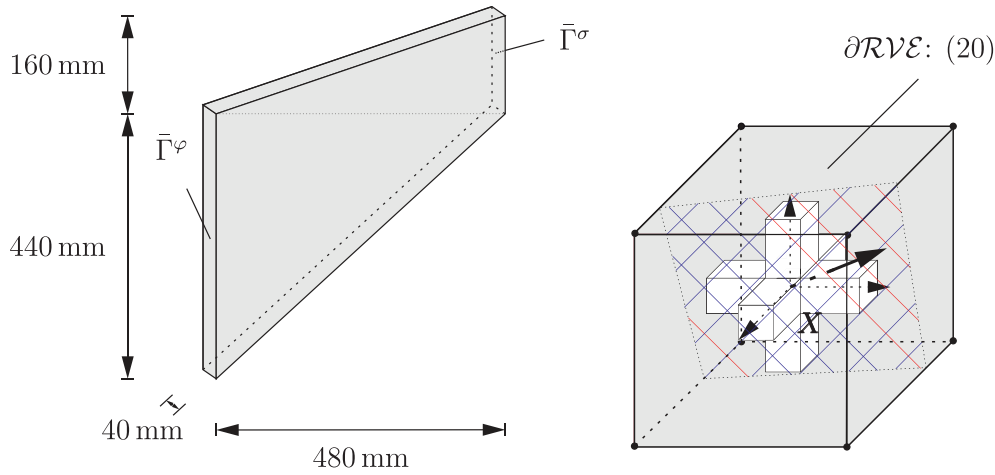
FIGURE 10 Cook's membrane. Left: Cook's membrane with Dirichlet boundaries $\overline{\Gamma}^{\varphi}$ on the left side and Neumann boundaries $\overline{\Gamma}^{\sigma}$ on the right side, right: $\mathcal{RVE}$ of the Cook's membrane with a second-gradient material for fiber-reinforced polymers with Dirichlet boundary conditions for the surfaces

B-splines on both scales with 27 Gauss points per element and set up two mesoscopic systems with $12 \times 12 \times 12$ and $24 \times 24 \times 24$ elements with in total 2744 and 17,576 control points, respectively. Since solving the $\mathcal{RVE}$ for all Gauss points of the macroscopic system in every load increment and Newton iteration requires a high computational effort, we applied a multigrid-solution scheme.

Remark 2. Multigrid-solution: For a fast and efficient solution, we construct a series of nested meshes on the macro- and mesoscale. Nested meshes are characterized by a linear dependency of the coarse shape functions from those of the fine scale. This can be easily constructed in the context of B-splines and NURBS, if the fine scale is constructed by a knot insertion technique (see, e.g., References 58 and 83). This technique provides all necessary topological information for the prolongation matrix $\mathbf{T}^{\text{pro}}$. Hence, a first simple algorithm for a fast solution as shown in Box 1 can be applied.

Note, that a further decrease of the computational effort can be obtained by using a series of nested meshes $M_{F_j}^{\text{RVE}}$ on the mesoscale as well for each macroscale M_{F_i}. Alternatively, the prolongation on the mesoscale can be circumvented by solving M_{F_i} with $M_{F_j}^{\text{RVE}}$ and prolongate to M_{F_i} itself but resolved with $M_{F_{j+1}}^{\text{RVE}}$. For the problem at hand, we solved

$$\left\{ M_{F_1} | M_{F_1}^{\text{RVE}} \right\} \xrightarrow{\mathbf{T}_{1,2}^{\text{pro}} \circ} \left\{ M_{F_2} | M_{F_1}^{\text{RVE}} \right\} \xrightarrow{\mathbf{T}_{2,2}^{\text{pro}} \circ} \left\{ M_{F_2} | M_{F_2}^{\text{RVE}} \right\} \xrightarrow{\mathbf{T}_{2,3}^{\text{pro}} \circ} \left\{ M_{F_3} | M_{F_2}^{\text{RVE}} \right\}.$$

BOX 1 Algorithm for fast solution using nested meshes

onstruct a coarse scale mesh M_{F_0}

for $i = 1 : n$, $n :=$ *number of elements* **do**

    Refine the mesh using a knot-insertion to obtain the fine mesh M_{F_i}.

    Construct prolongation matrix $\mathbf{T}_{i,i+1}^{\text{pro}}$.

end

for $i = 1 : n$ **do**

    Solve the multi-scale problem on M_{F_i}.

    Prolongate the solution $M_{F_{i+1}} = \mathbf{T}_{i,i+1}^{\text{pro}} \circ M_{F_i}$.

end

In Figure 11, we plotted the von Mises stress of selected levels of the multigrid-solution and additionally the norm of the second-order stress for the finest resolution of the macroscopic system with a scaled displacement. The second-order
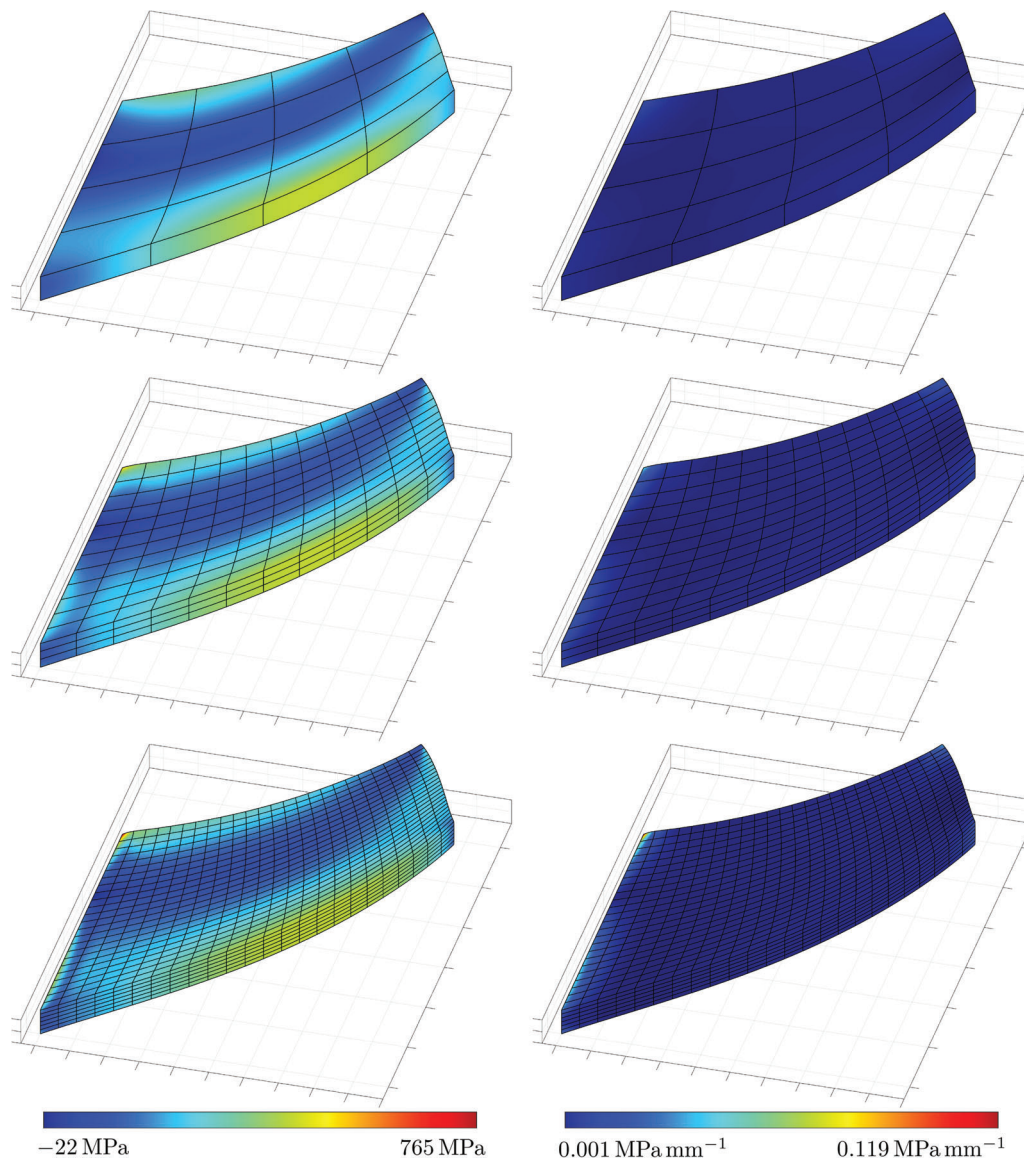
FIGURE 11 Cook's membrane. Stresses at different resolutions with a scaled displacement to the factor 5. Top to bottom: Level one, three, and four according to Table 4. Left to right: von Mises stress and $\|\mathfrak{P}\|$

TABLE 4 Cook's membrane: Computational effort and convergence

Level	1			2	3	4
Macro res.	$4 \times 4 \times 1$			$12 \times 12 \times 3$	$12 \times 12 \times 3$	$24 \times 24 \times 6$
Micro res.	$12 \times 12 \times 12$			$12 \times 12 \times 12$	$24 \times 24 \times 24$	$24 \times 24 \times 24$
Step	1/10	…	10/10	1/1	1/1	1/1
NR-iterations	1.64E + 04		1.63E + 04	3.30E + 05	3.96E + 02	1.03E + 05
	1.94E + 04		2.37E + 04	2.28E + 03	5.54E − 01	3.95E + 02
	4.12E + 00		1.17E + 00	8.95E − 01	2.03E − 04	2.47E − 01
	7.59E − 03		1.66E − 04	7.47E − 04	4.66E − 07	2.55E − 04
	7.30E − 06		8.93E − 07	8.90E − 07		6.73E − 07
$\sum \mathcal{RVE}$	21,600			58,320	46,656	466,560

Note: Newton–Raphson (NR) convergence utilizing the multigrid solution scheme on the macroscale and total number of solved $\mathcal{RVE}$ per multigrid level. Note that we conducted an incremental stepping on level one with 10 steps, whereas the load at higher levels was applied in a single step.

stress peaks in the area of clamped left side of the Cook's membrane and matches the expected behavior. Furthermore, Table 4 displays the convergence of the macroscopic system in each level of the multigrid-solution, indicating the accuracy of the linearization as proposed in Section 3.2. and demonstrating the computational effort.

5 | CONCLUSIONS

In this work, we could demonstrate a generalization for the numerical homogenization of higher-order strain gradient materials. This approach allows to homogenize first- and second-gradient materials on the mesoscale, containing representative quantities of the microstructure, toward second- and third-gradient materials on the macroscale. Suitable Dirichlet and periodic boundary conditions have been applied on the mesoscale to ensure an energetic consistent formulation, analogously to the Hill-Mandel criterion for first-gradient materials.

On both scales, the IGA concept using NURBS based shape functions has proven to be very well suited for these kind of formulations. Hence, we could implement an IGA^2-method and demonstrate the accuracy even for highly anisotropic strain gradient materials on the mesoscale. Eventually, we could derive a generalized framework for a consistent linearization of the macroscale values. The Newton-Raphson iteration for this highly nonlinear problem could be improved by calculating nested meshes on the micro- and the macroscale. With this framework at hand, novel computational investigations and predictions of the constitutive relations of materials with specific microstructures as now widely used in additive manufacturing are feasible.

ENDNOTES
*More strictly speaking, separation of scales is present when the wavelengths of physical fields at the higher scale are very much larger than the dimensions of heterogeneities at the lower scale.[1]

†Alternative schemes with even C^∞-continuous interpolations at the microscopic level have been proposed by Moulinec and Suquet [69] and were recently implemented in the framework of so-called FE-FFT methods. As the name suggests, associated schemes combine macroscopic solvers based on finite elements with microscopic solvers based on spectral methods (fast Fourier transforms; FFT), see References [70-72].

‡All appendices are written most generally with regard to a third-gradient medium. For the proposed second-gradient material, the corresponding terms of the third gradient can be removed easily.

§B-splines are used without loss of generality, NURBS can also be applied if necessary.

¶Setting the parameters strictly to zero may lead to numerical instabilities.

#Latin indices range in the set {1, 2, 3}. We will make use of the Einstein summation convention on repeated indices.

ORCID
Marc-André Keip 🔟 https://orcid.org/0000-0002-5838-5201
Christian Hesch 🔟 https://orcid.org/0000-0002-4614-2202

REFERENCES
1. Sanchez-Palencia E. Homogenization method for the study of composite media. In: Verhulst F, ed. *Asymptotic Analysis II. Lecture Notes in Mathematics*. Springer; 1983:192-214.
2. Cosserat E, Cosserat F. *Theorie des corps deformables*. A. Hermann et fils; 1909.
3. Toupin RA. Elastic materials with couple-stresses. *Arch Ration Mech Anal*. 1962;11(1):385-414.
4. Toupin RA. Theories of elasticity with couple-stress. *Arch Ration Mech Anal*. 1964;17(2):85-112.
5. Mindlin RD, Tiersten HF. Effects of couple-stresses in linear elasticity. *Arch Ration Mech Anal*. 1962;11(1):415-448.
6. Altenbach H, Eremeyev VA. Cosserat media. In: Altenbach H, Eremeyev VA, eds. *Generalized Continua from the Theory to Engineering Applications*. CISM International Centre for Mechanical Sciences. Springer; 2013:65-130.
7. Ehlers W, Bidier S. *Cosserat media. Encyclopedia of Continuum Mechanics*. Springer; 2020:436-446.
8. Eringen AC. Mechanics of micromorphic continua. In: Kröner E, ed. *Mechanics of Generalized Continua, IUTAM Symposia*. Springer; 1968:18-35.
9. Eringen AC. *Microcontinuum Field Theories: I. Foundations and Solids*. Springer Science & Business Media; 2012.
10. Hadjesfandiari AR, Dargush GF. Couple stress theory for solids. *Int J Solids Struct*. 2011;48(18):2496-2510.

11. Mindlin RD. Micro-structure in linear elasticity. *Arch Ration Mech Anal*. 1964;16(1):51-78.

12. Mindlin RD, Eshel NN. On first strain-gradient theories in linear elasticity. *Int J Solids Struct*. 1968;4(1):109-124.

13. Mindlin RD. Second gradient of strain and surface-tension in linear elasticity. *Int J Solids Struct*. 1965;1(4):417-438.

14. Germain P. The method of virtual power in continuum mechanics. Part 2: microstructure. *SIAM J Appl Math*. 1973;25(3):556-575.

15. Kirchner N, Steinmann P. A unifying treatise on variational principles for gradient and micromorphic continua. *Philos Mag*. 2005;85(33-35):3875-3895.

16. Javili A, dell'Isola F, Steinmann P. Geometrically nonlinear higher-gradient elasticity with energetic boundaries. *J Mech Phys Solids*. 2013;61(12):2381-2401.

17. Zervos A. Finite elements for elasticity with microstructure and gradient elasticity. *Int J Numer Methods Eng*. 2008;73(4):564-595.

18. Askes H, Aifantis EC. Gradient elasticity in statics and dynamics: an overview of formulations, length scale identification procedures, finite element implementations and new results. *Int J Solids Struct*. 2011;48(13):1962-1990.

19. Fischer P, Klassen M, Mergheim J, Steinmann P, Müller R. Isogeometric analysis of 2D gradient elasticity. *Comput Mech*. 2011;47(3):325-334.

20. Maugin GA, Metrikine AV. *Mechanics of Generalized Continua*. Springer; 2010.

21. Altenbach H, Maugin GA, Erofeev V. *Mechanics of Generalized Continua*. Vol 7. Springer; 2011.

22. Bertram A, Forest S. *Mechanics of Strain Gradient Materials*. Centro Internazionale di Scienze Meccaniche. Springer; 2020.

23. Aifantis EC. The physics of plastic deformation. *Int J Plasticity*. 1987;3(3):211-247.

24. Fleck NA, Muller GM, Ashby MF, Hutchinson JW. Strain gradient plasticity: theory and experiment. *Acta Metall Mater*. 1994;42(2):475-487.

25. Peerlings RHJ, de Borst R, Brekelmans WAM, De Vree JHP. Gradient enhanced damage for quasi-brittle materials. *Int J Numer Methods Eng*. 1996;39(19):3391-3403.

26. Miehe C. A multi-field incremental variational framework for gradient-extended standard dissipative solids. *J Mech Phys Solids*. 2011;59(4):898-923.

27. Hill R. The elastic behaviour of a crystalline aggregate. *Proc Phys Soc Sect A*. 1952;65(5):349.

28. Hashin Z, Shtrikman S. A variational approach to the theory of the elastic behaviour of multiphase materials. *J Mech Phys Solids*. 1963;11(2):127-140.

29. Hill R. A self-consistent mechanics of composite materials. *J Mech Phys Solids*. 1965;13(4):213-222.

30. Mori T, Tanaka K. Average stress in matrix and average elastic energy of materials with misfitting inclusions. *Acta Metall*. 1973;21(5):571-574.

31. Willis JR. Bounds and self-consistent estimates for the overall properties of anisotropic composites. *J Mech Phys Solids*. 1977;25:185-202.

32. Smit RJM, Brekelmans WAM, Meijer HEH. Prediction of the mechanical behavior of nonlinear heterogeneous systems by multi-level finite element modeling. *Comput Methods Appl Mech Eng*. 1998;155(1-2):181-192.

33. Miehe C, Schröder J, Schotte J. Computational homogenization analysis in finite plasticity simulation of texture development in polycrystalline materials. *Comput Methods Appl Mech Eng*. 1999;171(3-4):387-418.

34. Feyel F, Chaboche J-L. FE2 multiscale approach for modelling the elastoviscoplastic behaviour of long fibre SiC/Ti composite materials. *Comput Methods Appl Mech Eng*. 2000;183(3-4):309-330.

35. Kouznetsova VG, Brekelmans WAM, Baaijens FPT. An approach to micro-macro modeling of heterogeneous materials. *Comput Mech*. 2001;27(1):37-48.

36. Diener G, Hürrich A, Weissbarth J. Bounds on the non-local effective elastic properties of composites. *J Mech Phys Solids*. 1984;32(1):21-39.

37. Gambin B, Kröner E. Higher-order terms in the homogenized stress-strain relation of periodic elastic media. *Phys Status Solid B*. 1989;151(2):513-519.

38. Boutin C. Microstructural effects in elastic composites. *Int J Solids Struct*. 1996;33(7):1023-1051.

39. Drugan WJ, Willis JR. A micromechanics-based nonlocal constitutive equation and estimates of representative volume element size for elastic composites. *J Mech Phys Solids*. 1996;44(4):497-524.

40. Forest S. Homogenization methods and mechanics of generalized continua.-Part 2. *Theor Appl Mech*. 2002;28-29:113-144.

41. Hütter G. Homogenization of a Cauchy continuum towards a micromorphic continuum. *J Mech Phys Solids*. 2017;99:394-408.

42. Maurice G, Ganghoffer JF, Rahali Y. Second gradient homogenization of multilayered composites based on the method of oscillating functions. *Math Mech Solids*. 2019;24(7):2197-2230.

43. Ganghoffer JF, Maurice G, Rahali Y. Determination of closed form expressions of the second-gradient elastic moduli of multi-layer composites using the periodic unfolding method. *Math Mech Solids*. 2019;24(5):1475-1502.

44. Ganghoffer JF, Reda H. A variational approach of homogenization of heterogeneous materials towards second gradient continua. *Mech Mater*. 2021;158:103743.

45. Alavi SE, Ganghoffer JF, Reda H, Sadighi M. Construction of micromorphic continua by homogenization based on variational principles. *J Mech Phys Solids*. 2021;153:104278.

46. Bouyge F, Jasiuk I, Ostoja-Starzewski M. A micromechanically based couple–stress model of an elastic two-phase composite. *Int J Solids Struct*. 2001;38(10-13):1721-1735.

47. Feyel F. A multilevel finite element method (FE2) to describe the response of highly non-linear structures using generalized continua. *Comput Methods Appl Mech Eng*. 2003;192(28-30):3233-3244.

48. Jänicke R, Diebels S, Sehlhorst H-G, Düster A. Two-scale modelling of micromorphic continua. *Contin Mech Thermodyn*. 2009;21(4):297-315.

49. Rokoš O, Ameen MM, Peerlings RHJ, Geers MGD. Micromorphic computational homogenization for mechanical metamaterials with patterning fluctuation fields. *J Mech Phys Solids*. 2019;123:119-137.

50. Kouznetsova VG, Geers MGD, Brekelmans WAM. Multi-scale constitutive modelling of heterogeneous materials with a gradient-enhanced computational homogenization scheme. *Int J Numer Methods Eng*. 2002;54:1235-1260.

51. Kouznetsova VG, Geers MGD, Brekelmans WAM. Multi-scale second-order computational homogenization of multi-phase materials: a nested finite element solution strategy. *Comput Methods Appl Mech Eng*. 2004;193(48):5525-5550.

52. Bacigalupo A, Gambarotta L. Second-order computational homogenization of heterogeneous materials with periodic microstructure. *ZAMM-J Appl Math Mech/Zeitschrift für Angewandte Mathematik und Mechanik*. 2010;90(10-11):796-811.

53. Yvonnet J, Auffray N, Monchiet V. Computational second-order homogenization of materials with effective anisotropic strain-gradient behavior. *Int J Solids Struct*. 2020;191-192:434-448.

54. Forest S, Sab K. Cosserat overall modeling of heterogeneous materials. *Mech Res Commun*. 1998;25(4):449-454.

55. Forest S, Trinh DK. Generalized continua and non-homogeneous boundary conditions in homogenisation methods. *ZAMM-J Appl Math Mech/Zeitschrift für Angewandte Mathematik und Mechanik*. 2011;91(2):90-109.

56. Miehe C, Schotte J, Schröder J. Computational micro-macro transitions and overall moduli in the analysis of polycrystals at large strains. *Comput Mater Sci*. 1999;16(1-4):372-382.

57. Cirak F, Ortiz M, Schröder P. Subdivision surfaces: a new paradigm for thin-shell finite-element analysis. *Int J Numer Methods Eng*. 2000;47(12):2039-2072.

58. Hughes TJR, Cottrell JA, Bazilevs Y. Isogeometric analysis: CAD, finite elements, NURBS, exact geometry and mesh refinement. *Comput Methods Appl Mech Eng*. 2005;194(39–41):4135-4195.

59. Schulte J, Dittmann M, Eugster SR, et al. Isogeometric analysis of fiber reinforced composites using Kirchhoff–Love shell elements. *Comput Methods Appl Mech Eng*. 2020;362:112845.

60. Khristenko U, Schuß S, Krüger M, Schmidt F, Wohlmuth B, Hesch C. Multidimensional coupling: a variationally consistent approach to fiber-reinforced material. *Comput Methods Appl Mech Eng*. 2021;382:113869.

61. Schröder J, Keip M-A. Two-scale homogenization of electromechanically coupled boundary value problems. *Comput Mech*. 2012;50:229-244.

62. Keip M-A, Steinmann P, Schröder J. Two-scale computational homogenization of electro-elasticity at finite strains. *Comput Methods Appl Mech Eng*. 2014;278:62-79.

63. Keip M-A, Rambausek M. A multiscale approach to the computational characterization of magnetorheological elastomers. *Int J Numer Methods Eng*. 2016;107(4):338-360.

64. Schröder J. A numerical two-scale homogenization scheme: the FE2-method. In: Schröder J, Hackl K, eds. *Plasticity and Beyond. CISM International Centre for Mechanical Sciences,* Vol 550. 2014; Springer.

65. Matouš K, Geers MGD, Kouznetsova VG, Gillman A. A review of predictive nonlinear theories for multiscale modeling of heterogeneous materials. *J Comput Phys*. 2017;330:192-220.

66. Brezzi F, Fortin M. *Mixed and Hybrid Finite Element Methods*. Springer-Verlag; 1991.

67. Teichtmeister S, Kienle D, Aldakheel F, Keip M-A. Phase field modeling of fracture in anisotropic brittle solids. *Int J Non-Linear Mech*. 2017;97:1-21.

68. Crouzeix M, Raviart P-A. Conforming and nonconforming finite element methods for solving the stationary Stokes equations I. *ESAIM Math Model Numer Anal Modélisation Mathématique et Analyse Numérique*. 1973;7(R3):33-75.

69. Moulinec H, Suquet P. A numerical method for computing the overall response of nonlinear composites with complex microstructure. *Comput Methods Appl Mech Eng*. 1998;157(1-2):69-94.

70. Spahn J, Andrä H, Kabel M, Müller R. A multiscale approach for modeling progressive damage of composite materials using fast Fourier transforms. *Comput Methods Appl Mech Eng*. 2014;268:871-883.

71. Kochmann J, Wulfinghoff S, Reese S, Mianroodi JR, Svendsen B. Two-scale FE–FFT-and phase-field-based computational modeling of bulk microstructural evolution and macroscopic material behavior. *Comput Methods Appl Mech Eng*. 2016;305:89-110.

72. Göküzüm FS, Keip M-A. An algorithmically consistent macroscopic tangent operator for FFT-based computational homogenization. *Int J Numer Methods Eng*. 2018;113(4):581-600.

73. Alberdi R, Zhang G, Khandelwal K. A framework for implementation of RVE-based multiscale models in computational homogenization using isogeometric analysis. *Int J Numer Methods Eng*. 2018;114(9):1018-1051.

74. Wang Z-P, Poh LH. Optimal form and size characterization of planar isotropic petal-shaped auxetics with tunable effective properties using IGA. *Compos Struct*. 2018;201:486-502.

75. Kouznetsova VG. *Computational Homogenization for the Multi-Scale Analysis of Multi-phase Materials*. Ph.D. thesis. Technische Universiteit Eindhoven; 2002.

76. Dittmann M, Schulte J, Schmidt F, Hesch C. A strain-gradient formulation for fiber reinforced polymers: hybrid phase-field model for porous-ductile fracture. *Comput Mech*. 2021;67:1747-1768.

77. Madeo A, Ghiba I-D, Neff P, Münch I. A new view on boundary conditions in the Grioli–Koiter–Mindlin–Toupin indeterminate couple stress model. *Eur J Mech A*. 2016;59:294-322.

78. Schuß S, Dittmann M, Wohlmuth B, Klinkel S, Hesch C. Multi-patch isogeometric analysis for Kirchhoff–Love shell elements. *Comput Methods Appl Mech Eng*. 2019;349:91-116.

79. Dittmann M, Schuß S, Wohlmuth B, Hesch C. Weak C^n coupling for multi-patch isogeometric analysis in solid mechanics. *Int J Numer Methods Eng*. 2019;118:678-699.

80. Dittmann M, Schuß S, Wohlmuth B, Hesch C. Crosspoint modification for multi-patch isogeometric analysis. *Comput Methods Appl Mech Eng*. 2020;360:112768.

81. Cottrell JA, Hughes TJR, Bazilevs Y. *Isogeometric Analysis: Toward Integration of CAD and FEA*. Wiley; 2009.

82. Asmanoglo T, Menzel A. A finite deformation continuum modelling framework for curvature effects in fibre-reinforced nanocomposites. *J Mech Phys Solids*. 2017;107:411-432.

83. Piegl L, Tiller W. *The NURBS Book*. 2nd ed. Springer; 2010.

APPENDICES

The article summarizes all necessary equations for a second-gradient micro- and macrocontinuum. In Remark 1, we discuss the combination of a second-gradient microcontinuum and a third-gradient macrocontinuum. Therefore, we write Appendices B–D for the latter one. Omitting the fourth-order tensor $\overline{\mathbb{F}} = \overline{\nabla}^3 \overline{\boldsymbol{\varphi}}$ and the triple stress tensor $\overline{\mathbb{P}}$, we end up in the equations for the second-gradient micro- and macrocontinuum mainly used in the article.

APPENDIX A. NOTATION

In the following, we briefly summarize the notation mainly used. The scalar product of two vectors $\boldsymbol{a}, \boldsymbol{b}$, two second-order tensors $\boldsymbol{A}, \boldsymbol{B}$, two third-order tensors $\mathfrak{A}, \mathfrak{B}$, and two fourth-order tensors $\mathbb{A}, \mathbb{B}$ is given by[#]

$$[\boldsymbol{a} \cdot \boldsymbol{b}] = a_i \, b_i \, , \quad [\boldsymbol{A} : \boldsymbol{B}] = A_{ij} \, B_{ij} \, , \quad [\mathfrak{A} \, \vdots \, \mathfrak{B}] = A_{ijk} \, B_{ijk} \, , \quad [\mathbb{A} :: \mathbb{B}] = A_{ijkl} \, B_{ijkl}. \tag{A1}$$

Other multiplications of two tensors of different order are given in the following way, here for example, for a fourth-order tensor $\mathbb{A}$ with a third-order tensor $\mathfrak{B}$, second-order tensor $\boldsymbol{B}$ and vector $\boldsymbol{b}$, respectively

$$[\mathbb{A} \, \boldsymbol{b}]_{ijk} = A_{ijkl} \, b_l \, , \quad [\mathbb{A} : \boldsymbol{B}]_{ij} = A_{ijkl} \, B_{kl} \, , \quad [\mathbb{A} \, \vdots \, \mathfrak{B}]_i = A_{ijkl} \, B_{jkl}. \tag{A2}$$

All other combinations follow analogously. The dyadic product $\otimes$ increases the order of the tensor. For example, a dyadic product of two vectors $\boldsymbol{a}, \boldsymbol{b}$ is given by $\boldsymbol{A} = \boldsymbol{a} \otimes \boldsymbol{b}$ with $A_{ij} = a_i \, b_j$. Next, we define the macroscopic gradient with respect to the macroscopic reference configuration $\overline{\nabla}(\bullet)$ of a vector field $\overline{\boldsymbol{a}}$ and of a second-order tensor field $\overline{\boldsymbol{A}}$ as

$$[\overline{\nabla}\overline{\boldsymbol{a}}]_{iJ} = \frac{\partial [\overline{\boldsymbol{a}}]_i}{\partial [\overline{\boldsymbol{X}}]_J} \quad \text{and} \quad [\overline{\nabla}\overline{\boldsymbol{A}}]_{iJK} = \frac{\partial [\overline{\boldsymbol{A}}]_{iJ}}{\partial [\overline{\boldsymbol{X}}]_K}. \tag{A3}$$

For the macroscopic divergence operator, it follows

$$[\overline{\nabla} \cdot \overline{\boldsymbol{A}}]_i = \frac{\partial [\overline{\boldsymbol{A}}]_{iJ}}{\partial [\overline{\boldsymbol{X}}]_J} \quad \text{and} \quad [\overline{\boldsymbol{\nabla}} \cdot \overline{\mathfrak{A}}]_{iJ} = \frac{\partial [\overline{\mathfrak{A}}]_{iJK}}{\partial [\overline{\boldsymbol{X}}]_K}. \tag{A4}$$

The microscopic gradient $\nabla \boldsymbol{a}$ and $\nabla \boldsymbol{A}$ as well as the divergence operators $\nabla \cdot \boldsymbol{A}$ and $\nabla \cdot \mathfrak{A}$ are given analogously to (A3) and (A4) omitting the overlined symbol " $^-$ ". Furthermore, the transpose $^{\mathrm{T}i}$ with number $i = 1, 2, 3$ denotes the number of shifted reference magnitudes

$$[\boldsymbol{A}]_{iJ} = [[\boldsymbol{A}]_{Ji}]^{\mathrm{T}1} = [[\boldsymbol{A}]_{Ji}]^{\mathrm{T}} \, , \quad [\mathfrak{A}]_{iJK} = \left[[\mathfrak{A}]_{KiJ}\right]^{\mathrm{T}1} , \quad [\mathfrak{A}]_{iJK} = \left[[\mathfrak{A}]_{JKi}\right]^{\mathrm{T}2},$$
$$[\mathbb{A}]_{iJKL} = \left[[\mathbb{A}]_{KLiJ}\right]^{\mathrm{T}2} , \qquad\qquad [\mathbb{A}]_{iJKL} = \left[[\mathbb{A}]_{JKLi}\right]^{\mathrm{T}3}. \tag{A5}$$

Furthermore, we have to interchange some reference indices with $^{\mathrm{C}ij}$, where i, j denote the indices which will be interchanged

$$\left[\mathfrak{A}\right]_{JKi} = \left[\left[\mathfrak{A}\right]_{KJi}\right]^{C12}, \qquad \left[\mathbb{A}\right]_{KLiJ} = \left[\left[\mathfrak{A}\right]_{LKiJ}\right]^{C12},$$

$$\left[\mathbb{A}\right]_{JKLi} = \left[\left[\mathfrak{A}\right]_{LKJi}\right]^{C13}, \qquad \left[\mathbb{A}\right]_{JKLi} = \left[\left[\mathfrak{A}\right]_{JLKi}\right]^{C23}. \tag{A6}$$

APPENDIX B. MACROSCOPIC KINEMATIC

The microscopic kinematic for the third-gradient macroscopic continuum is given by

$$\boldsymbol{\varphi}(\boldsymbol{X}) = \overline{\boldsymbol{F}}\,\boldsymbol{X} + \frac{1}{2}\,\overline{\mathfrak{F}} : (\boldsymbol{X} \otimes \boldsymbol{X}) + \frac{1}{6}\,\overline{\mathbb{F}} \vdots (\boldsymbol{X} \otimes \boldsymbol{X} \otimes \boldsymbol{X}) + \tilde{\boldsymbol{w}}. \tag{B1}$$

The connections between the macroscopic deformations and the averaged microscopic deformations are given by

$$\frac{1}{V}\int_{\mathcal{RVE}} \boldsymbol{F}\,\mathrm{d}V = \frac{1}{V}\int_{\mathcal{RVE}} \left(\overline{\boldsymbol{F}} + \overline{\mathfrak{F}}\,\boldsymbol{X} + \frac{1}{2}\,\overline{\mathbb{F}} : (\boldsymbol{X} \otimes \boldsymbol{X}) + \tilde{\boldsymbol{F}}\right)\,\mathrm{d}V$$

$$= \overline{\boldsymbol{F}} + \overline{\mathbb{F}} : \frac{1}{V}\int_{\mathcal{RVE}} \frac{1}{2}\,(\boldsymbol{X} \otimes \boldsymbol{X})\,\mathrm{d}V \tag{B2}$$

and

$$\frac{1}{V}\int_{\mathcal{RVE}} \mathfrak{F}\,\mathrm{d}V = \frac{1}{V}\int_{\mathcal{RVE}} \left(\overline{\mathfrak{F}} + \overline{\mathbb{F}}\,\boldsymbol{X} + \tilde{\mathfrak{F}}\right)\,\mathrm{d}V = \overline{\mathfrak{F}} \tag{B3}$$

using $\int_{\mathcal{RVE}} \boldsymbol{X}\mathrm{d}V = \boldsymbol{0}$, which is valid if the coordinate system is in the center of the $\mathcal{RVE}$. Furthermore, $\tilde{\boldsymbol{F}} = \nabla\tilde{\boldsymbol{w}}$ and $\tilde{\mathfrak{F}} = \nabla^2\tilde{\boldsymbol{w}}$ are the first and second gradients of the fluctuation field. Since the macroscopic values are exactly the volume averages of the microscopic values and not dependent on the fluctuations, we can write

$$\frac{1}{V}\int_{\mathcal{RVE}} \nabla\tilde{\boldsymbol{w}}\,\mathrm{d}V = \boldsymbol{0} \quad \text{and} \quad \frac{1}{V}\int_{\mathcal{RVE}} \nabla^2\tilde{\boldsymbol{w}}\,\mathrm{d}V = \langle. \tag{B4}$$

Using Gauss's theorem, we can rewrite the volume integrals of (B4) to surface integrals:

$$\frac{1}{V}\int_{\partial\mathcal{RVE}} \tilde{\boldsymbol{w}} \otimes \boldsymbol{N}\,\mathrm{d}A = \boldsymbol{0} \quad \text{and} \quad \frac{1}{V}\int_{\partial\mathcal{RVE}} \nabla\tilde{\boldsymbol{w}} \otimes \boldsymbol{N}\,\mathrm{d}A = \langle. \tag{B5}$$

using the divergence theorem for a unit tensor $\boldsymbol{I}$ and a vector $\boldsymbol{a}$

$$\int_{\partial\mathcal{RVE}} \boldsymbol{a} \cdot (\boldsymbol{I}\,\boldsymbol{N})\,\mathrm{d}A = \int_{\mathcal{RVE}} \nabla \cdot (\boldsymbol{I}^{\mathrm{T}}\,\boldsymbol{a})\,\mathrm{d}V,$$

$$\boldsymbol{I} : \int_{\partial\mathcal{RVE}} \boldsymbol{a} \otimes \boldsymbol{N}\,\mathrm{d}A = \int_{\mathcal{RVE}} \underbrace{(\nabla \cdot \boldsymbol{I})}_{\boldsymbol{0}} \cdot \boldsymbol{a}\,\mathrm{d}V + \boldsymbol{I} : \int_{\mathcal{RVE}} \nabla\boldsymbol{a}\,\mathrm{d}V, \tag{B6}$$

or for a tensor $\boldsymbol{A}$ and the unit tensor $\boldsymbol{I}$

$$\int_{\partial\mathcal{RVE}} (\boldsymbol{A}\,\boldsymbol{I})\,\boldsymbol{N}\,\mathrm{d}A = \int_{\mathcal{RVE}} \nabla \cdot (\boldsymbol{A}\,\boldsymbol{I})\,\mathrm{d}V,$$

$$\int_{\partial\mathcal{RVE}} \boldsymbol{A} \otimes \boldsymbol{N}\,\mathrm{d}A : \boldsymbol{I} = \int_{\mathcal{RVE}} \nabla\boldsymbol{A}\,\mathrm{d}V : \boldsymbol{I} + \int_{\mathcal{RVE}} \boldsymbol{A}\,\underbrace{(\nabla \cdot \boldsymbol{I})}_{\boldsymbol{0}}\,\mathrm{d}V, \tag{B7}$$

respectively.

APPENDIX C. MACROSCOPIC STRESSES

For the derivation of the macroscopic stresses, we use the partial integration and the Gaussian integral theorem for the integral of the left side of the energetic criterion (22):

$$
\begin{aligned}
\int_{\mathcal{RVE}} & \left(\boldsymbol{P} : \nabla \delta \boldsymbol{\varphi} + \mathfrak{P} \,\vdots\, \nabla^2 \delta \boldsymbol{\varphi} \right) \, \mathrm{d}V \\
&= \int_{\mathcal{RVE}} \nabla \cdot \left([\boldsymbol{P} - \nabla \cdot \mathfrak{P}]^{\mathrm{T}} \, \delta \boldsymbol{\varphi} + \mathfrak{P}^{\mathrm{T1}} : \nabla \delta \boldsymbol{\varphi} \right) \, \mathrm{d}V - \int_{\mathcal{RVE}} \underbrace{\left(\nabla \cdot [\boldsymbol{P} - \nabla \cdot \mathfrak{P}] \right)}_{=\boldsymbol{0}} \cdot \delta \boldsymbol{\varphi} \, \mathrm{d}V \\
&= \int_{\partial \mathcal{RVE}} \left([(\boldsymbol{P} - \nabla \cdot \mathfrak{P}) \, \boldsymbol{N}] \cdot \delta \boldsymbol{\varphi} + [\mathfrak{P} \, \boldsymbol{N}] : \nabla \delta \boldsymbol{\varphi} \right) \, \mathrm{d}A.
\end{aligned}
\tag{C1}
$$

The macroscopic stresses are defined in terms of surface integrals since macroscopic values defined by volume integrals could lead to nonphysical results, see Schröder and Keip.[61] Inserting the variations of the material points $\boldsymbol{\varphi}$:

$$
\delta \boldsymbol{\varphi} = \delta \overline{\boldsymbol{F}} \, \boldsymbol{X} + \frac{1}{2} \, \delta \overline{\mathfrak{F}} : (\boldsymbol{X} \otimes \boldsymbol{X}) + \frac{1}{6} \, \delta \overline{\mathbb{F}} \,\vdots\, (\boldsymbol{X} \otimes \boldsymbol{X} \otimes \boldsymbol{X}) + \delta \tilde{\boldsymbol{w}}
\tag{C2}
$$

and

$$
\nabla \delta \boldsymbol{\varphi} = \delta \overline{\boldsymbol{F}} + \delta \overline{\mathfrak{F}} \, \boldsymbol{X} + \frac{1}{2} \, \delta \overline{\mathbb{F}} : (\boldsymbol{X} \otimes \boldsymbol{X}) + \delta \tilde{\boldsymbol{F}}
\tag{C3}
$$

in the last equation, we can split the integral into three parts depending on the variation of the macroscopic deformation gradient $\overline{\boldsymbol{F}}$, the second gradient $\overline{\mathfrak{F}}$ and the third gradient $\overline{\mathbb{F}}$:

$$
\begin{aligned}
\int_{\mathcal{RVE}} & \left(\boldsymbol{P} : \nabla \delta \boldsymbol{\varphi} + \mathfrak{P} \,\vdots\, \nabla^2 \delta \boldsymbol{\varphi} \right) \mathrm{d}V \\
&= \int_{\partial \mathcal{RVE}} \left(\mathfrak{P} \, \boldsymbol{N} + [\boldsymbol{P} - \nabla \cdot \mathfrak{P}] \, \boldsymbol{N} \otimes \boldsymbol{X} \right) \, \mathrm{d}A : \delta \overline{\boldsymbol{F}} \\
&\quad + \int_{\partial \mathcal{RVE}} \left(\mathfrak{P} \, \boldsymbol{N} \otimes \boldsymbol{X} + \frac{1}{2} \, [\boldsymbol{P} - \nabla \cdot \mathfrak{P}] \, \boldsymbol{N} \otimes \boldsymbol{X} \otimes \boldsymbol{X} \right) \, \mathrm{d}A \,\vdots\, \delta \overline{\mathfrak{F}} \\
&\quad + \int_{\partial \mathcal{RVE}} \left(\frac{1}{2} \, \mathfrak{P} \, \boldsymbol{N} \otimes \boldsymbol{X} \otimes \boldsymbol{X} + \frac{1}{6} \, [\boldsymbol{P} - \nabla \cdot \mathfrak{P}] \, \boldsymbol{N} \otimes \boldsymbol{X} \otimes \boldsymbol{X} \otimes \boldsymbol{X} \right) \, \mathrm{d}A \,\vdots\vdots\, \delta \overline{\mathbb{F}}
\end{aligned}
\tag{C4}
$$

with the restrictions on the boundary, since the macroscopic stresses are not dependent on the fluctuations:

$$
\int_{\partial \mathcal{RVE}} (\mathfrak{P} \, \boldsymbol{N}) : \nabla \delta \tilde{\boldsymbol{w}} \, \mathrm{d}A = 0 \quad \text{and} \quad \int_{\partial \mathcal{RVE}} [(\boldsymbol{P} - \nabla \cdot \mathfrak{P}) \, \boldsymbol{N}] \cdot \delta \tilde{\boldsymbol{w}} \, \mathrm{d}A = 0.
\tag{C5}
$$

The transformation back to volume integrals leads to:

$$
\begin{aligned}
\int_{\mathcal{RVE}} & \left(\boldsymbol{P} : \nabla \delta \boldsymbol{\varphi} + \mathfrak{P} \,\vdots\, \nabla^2 \delta \boldsymbol{\varphi} \right) \mathrm{d}V \\
&= \int_{\mathcal{RVE}} \left(\nabla \cdot \mathfrak{P} + [\nabla \cdot (\boldsymbol{X} \otimes [\boldsymbol{P} - \nabla \cdot \mathfrak{P}])]^{\mathrm{T}} \right) \, \mathrm{d}V : \delta \overline{\boldsymbol{F}} \\
&\quad + \int_{\mathcal{RVE}} \left([\nabla \cdot (\boldsymbol{X} \otimes \mathfrak{P})]^{\mathrm{T1}} + \frac{1}{2} \, [\nabla \cdot (\boldsymbol{X} \otimes \boldsymbol{X} \otimes [\boldsymbol{P} - \nabla \cdot \mathfrak{P}])]^{\mathrm{T2}} \right) \, \mathrm{d}V \,\vdots\, \delta \overline{\mathfrak{F}}
\end{aligned}
$$

$$
\begin{aligned}
&+ \int_{\mathcal{RVE}} \left(\frac{1}{2} \left[\nabla \cdot (\boldsymbol{X} \otimes \boldsymbol{X} \otimes \mathfrak{P}) \right]^{T2} + \frac{1}{6} \left[\nabla \cdot (\boldsymbol{X} \otimes \boldsymbol{X} \otimes \boldsymbol{X} \otimes [\boldsymbol{P} - \nabla \cdot \mathfrak{P}]) \right]^{T3} \right) \, \mathrm{d}V :: \delta \overline{\mathbb{F}} \\
&= \int_{\mathcal{RVE}} \boldsymbol{P} \, \mathrm{d}V : \delta \overline{\boldsymbol{F}} + \int_{\mathcal{RVE}} \left(\mathfrak{P} + \nabla \cdot \mathfrak{P} \otimes \boldsymbol{X} + [\boldsymbol{P} - \nabla \cdot \mathfrak{P}] \otimes \boldsymbol{X} \right) \, \mathrm{d}V \; : \; \delta \overline{\mathfrak{F}} \\
&\quad + \int_{\mathcal{RVE}} \left(\mathfrak{P} \otimes \boldsymbol{X} + \frac{1}{2} \nabla \cdot \mathfrak{P} \otimes \boldsymbol{X} \otimes \boldsymbol{X} + \frac{1}{2} [\boldsymbol{P} - \nabla \cdot \mathfrak{P}] \otimes \boldsymbol{X} \otimes \boldsymbol{X} \right) \, \mathrm{d}V :: \delta \overline{\mathbb{F}} \\
&= \int_{\mathcal{RVE}} \boldsymbol{P} \, \mathrm{d}V : \delta \overline{\boldsymbol{F}} + \int_{\mathcal{RVE}} \left(\mathfrak{P} + \boldsymbol{P} \otimes \boldsymbol{X} \right) \, \mathrm{d}V \; : \; \delta \overline{\mathfrak{F}} \\
&\quad + \int_{\mathcal{RVE}} \left(\mathfrak{P} \otimes \boldsymbol{X} + \frac{1}{2} \boldsymbol{P} \otimes \boldsymbol{X} \otimes \boldsymbol{X} \right) \, \mathrm{d}V :: \delta \overline{\mathbb{F}},
\end{aligned}
\tag{C6}
$$

where we used the following equalities for the divergence of third-, fourth-, and fifth-order tensors:

$$
\begin{aligned}
\nabla \cdot (\boldsymbol{X} \otimes \boldsymbol{A}) &= \boldsymbol{A}^{\mathrm{T}} + \boldsymbol{X} \otimes \nabla \cdot \boldsymbol{A}, \\
\nabla \cdot (\boldsymbol{X} \otimes \mathfrak{A}) &= \mathfrak{A}^{\mathrm{T1}} + \boldsymbol{X} \otimes \nabla \cdot \mathfrak{A}, \\
\nabla \cdot (\boldsymbol{X} \otimes \boldsymbol{X} \otimes \boldsymbol{A}) &= \left(\boldsymbol{X} \otimes \boldsymbol{A}^{\mathrm{T}} \right)^{\mathrm{C12}} + \boldsymbol{X} \otimes \boldsymbol{A}^{\mathrm{T}} + \boldsymbol{X} \otimes \boldsymbol{X} \otimes \nabla \cdot \boldsymbol{A}, \\
\nabla \cdot (\boldsymbol{X} \otimes \boldsymbol{X} \otimes \mathfrak{A}) &= \left(\boldsymbol{X} \otimes \mathfrak{A}^{\mathrm{T1}} \right)^{\mathrm{C12}} + \boldsymbol{X} \otimes \mathfrak{A}^{\mathrm{T1}} + \boldsymbol{X} \otimes \boldsymbol{X} \otimes \nabla \cdot \mathfrak{A}, \\
\nabla \cdot (\boldsymbol{X} \otimes \boldsymbol{X} \otimes \boldsymbol{X} \otimes \boldsymbol{A}) &= \left(\boldsymbol{X} \otimes \boldsymbol{X} \otimes \boldsymbol{A}^{\mathrm{T}} \right)^{\mathrm{C13}} + \left(\boldsymbol{X} \otimes \boldsymbol{X} \otimes \boldsymbol{A}^{\mathrm{T}} \right)^{\mathrm{C23}} + \boldsymbol{X} \otimes \boldsymbol{X} \otimes \boldsymbol{A}^{\mathrm{T}} \\
&\quad + \boldsymbol{X} \otimes \boldsymbol{X} \otimes \boldsymbol{X} \otimes \nabla \cdot \boldsymbol{A},
\end{aligned}
\tag{C7}
$$

as well as the strong form of the second-gradient microscopic continuum (14), the symmetry of $\left[\overline{\mathfrak{F}} \right]_{iJK}$ in J, K and the symmetry of $\left[\overline{\mathbb{F}} \right]_{iJKL}$ in J, K, L.

APPENDIX D. MESOSCOPIC BOUNDARY CONDITIONS

For the third-gradient macroscopic continuum, we can rewrite the energetic criterion (22) as

$$
\begin{aligned}
\frac{1}{V} \int_{\mathcal{RVE}} \left[\overline{\boldsymbol{P}} - \boldsymbol{P} \right] &: \left[\delta \overline{\boldsymbol{F}} + \delta \overline{\mathfrak{F}} \, \boldsymbol{X} + \frac{1}{2} \delta \overline{\mathbb{F}} : (\boldsymbol{X} \otimes \boldsymbol{X}) - \delta \boldsymbol{F} \right] \, \mathrm{d}V \\
&+ \frac{1}{V} \int_{\mathcal{RVE}} \left[\overline{\mathfrak{P}}^{\mathfrak{P}} - \mathfrak{P} \right] \; : \; \left[\delta \overline{\mathfrak{F}} + \delta \overline{\mathbb{F}} \, \boldsymbol{X} - \delta \mathfrak{F} \right] \, \mathrm{d}V = 0,
\end{aligned}
\tag{D1}
$$

to obtain more information about the boundary conditions. Obviously, the simplest assumption for all points of the microscopic scale, that fulfills the last equation is given by postulating the constraints $\overline{\boldsymbol{P}} := \boldsymbol{P}$ or $\delta \overline{\boldsymbol{F}} + \delta \overline{\mathfrak{F}} \, \boldsymbol{X} + \frac{1}{2} \delta \overline{\mathbb{F}} : (\boldsymbol{X} \otimes \boldsymbol{X}) = \delta \boldsymbol{F}$ and additionally $\overline{\mathfrak{P}}^{\mathfrak{P}} := \mathfrak{P}$ or $\delta \overline{\mathfrak{F}} + \delta \overline{\mathbb{F}} \, \boldsymbol{X} = \delta \mathfrak{F}$, compare Schröder.[64]

D.1 Proof of further representation of energetic criterion
For the derivation of the boundary condition, we have to show, that the energetic criterion (22) is equal to (D1). The first term of (D1) leads to

$$
\begin{aligned}
\frac{1}{V} \int_{\mathcal{RVE}} \left[\overline{\boldsymbol{P}} - \boldsymbol{P} \right] &: \left[\delta \overline{\boldsymbol{F}} + \delta \overline{\mathfrak{F}} \, \boldsymbol{X} + \frac{1}{2} \delta \overline{\mathbb{F}} : (\boldsymbol{X} \otimes \boldsymbol{X}) - \delta \boldsymbol{F} \right] \, \mathrm{d}V \\
&= - \overline{\boldsymbol{P}} : \delta \overline{\boldsymbol{F}} - \overline{\mathfrak{P}}^{P} \; : \; \delta \overline{\mathfrak{F}} - \overline{\mathbb{P}}^{P} :: \delta \overline{\mathbb{F}} + \frac{1}{V} \int_{\mathcal{RVE}} \boldsymbol{P} : \delta \boldsymbol{F} \, \mathrm{d}V,
\end{aligned}
\tag{D2}
$$

taking advantage of the fact that the macroscopic quantities are constant over the volume of the $\mathcal{RVE}$ and $\frac{1}{V} \int_{\mathcal{RVE}} X dV = \mathbf{0}$, if the coordinate system is in the center of the $\mathcal{RVE}$. Furthermore, the correlations between the microscopic and macroscopic quantities (B2) and (24) are used. For the second term of (D1), we use additionally (B3), which leads to

$$\frac{1}{V} \int_{\mathcal{RVE}} \left[\overline{\mathfrak{P}}^{\mathfrak{B}} - \mathfrak{P} \right] \; \vdots \; \left[\delta\overline{\mathfrak{F}} + \delta\overline{\mathbb{F}} \, X - \delta\mathfrak{F} \right] dV = -\overline{\mathfrak{P}}^{\mathfrak{B}} \; \vdots \; \delta\overline{\mathfrak{F}} - \overline{\mathbb{P}}^{\mathfrak{B}} \; \vdots \; \delta\overline{\mathbb{F}} + \frac{1}{V} \int_{\mathcal{RVE}} \mathfrak{P} \; \vdots \; \delta\mathfrak{F} \, dV. \tag{D3}$$

So, we can write for (18) by adding the last two equations

$$\frac{1}{V} \int_{\mathcal{RVE}} \boldsymbol{P} : \delta\boldsymbol{F} \, dV + \frac{1}{V} \int_{\mathcal{RVE}} \mathfrak{P} \; \vdots \; \delta\mathfrak{F} \, dV = \overline{\boldsymbol{P}} : \delta\overline{\boldsymbol{F}} + \left(\overline{\mathfrak{P}}^{\mathfrak{B}} + \overline{\mathfrak{P}}^{P} \right) \; \vdots \; \delta\overline{\mathfrak{F}} + \left(\overline{\mathbb{P}}^{\mathfrak{B}} + \overline{\mathbb{P}}^{P} \right) \; \vdots \; \delta\overline{\mathbb{F}}, \tag{D4}$$

which reflects the energetic criterion (22).

D.2 Boundary integral of energetic criterion

Here, the transfer of the volume integrals of (D1) to boundary integrals of the energetic criterion is explained. Using the partial integration for the first and second term of (D1), we get for the first term

$$\frac{1}{V} \int_{\mathcal{RVE}} \left[\overline{\boldsymbol{P}} - \boldsymbol{P} \right] : \left[\delta\overline{\boldsymbol{F}} + \delta\overline{\mathfrak{F}} \, X + \frac{1}{2} \delta\overline{\mathbb{F}} : (X \otimes X) - \delta\boldsymbol{F} \right] dV$$

$$= \frac{1}{V} \int_{\mathcal{RVE}} \nabla \cdot \left(\left[\overline{\boldsymbol{P}} - \boldsymbol{P} \right]^{\mathrm{T}} \left[\delta\overline{\boldsymbol{F}} \, X + \frac{1}{2} \delta\overline{\mathfrak{F}} : (X \otimes X) + \frac{1}{6} \delta\overline{\mathbb{F}} \; \vdots \; (X \otimes X \otimes X) - \delta\boldsymbol{\varphi} \right] \right) dV \tag{D5}$$

$$+ \frac{1}{V} \int_{\mathcal{RVE}} \nabla \cdot \boldsymbol{P} \cdot \left[\delta\overline{\boldsymbol{F}} \, X + \frac{1}{2} \delta\overline{\mathfrak{F}} : (X \otimes X) + \frac{1}{6} \delta\overline{\mathbb{F}} \; \vdots \; (X \otimes X \otimes X) - \delta\boldsymbol{\varphi} \right] dV,$$

with $\nabla \cdot \overline{\boldsymbol{P}} = \mathbf{0}$ and analogously for the second term

$$\frac{1}{V} \int_{\mathcal{RVE}} \left[\overline{\mathfrak{P}}^{\mathfrak{B}} - \mathfrak{P} \right] \; \vdots \; \left[\delta\overline{\mathfrak{F}} + \delta\overline{\mathbb{F}} \, X - \delta\mathfrak{F} \right] dV$$

$$= \frac{1}{V} \int_{\mathcal{RVE}} \nabla \cdot \left(\left[\overline{\mathfrak{P}}^{\mathfrak{B}} - \mathfrak{P} \right]^{\mathrm{T1}} : \left[\delta\overline{\mathfrak{F}} \, X + \frac{1}{2} \delta\overline{\mathbb{F}} : (X \otimes X) - \delta\boldsymbol{F} \right] \right) dV \tag{D6}$$

$$+ \frac{1}{V} \int_{\mathcal{RVE}} \nabla \cdot \mathfrak{P} : \left[\delta\overline{\mathfrak{F}} \, X + \frac{1}{2} \delta\overline{\mathbb{F}} : (X \otimes X) - \delta\boldsymbol{F} \right] dV,$$

with $\nabla \cdot \overline{\mathfrak{P}} = \mathbf{0}$. Now, adding the following zero term

$$\frac{1}{V} \int_{\mathcal{RVE}} \left(\nabla \cdot \left(\left[\overline{\mathfrak{P}}^{\mathfrak{B}} - \mathfrak{P} \right]^{\mathrm{T1}} : \delta\overline{\boldsymbol{F}} \right) + \nabla \cdot \mathfrak{P} : \delta\overline{\boldsymbol{F}} \right) dV = 0, \tag{D7}$$

to the right-hand side of (D6) leads only to a change of (D6) in the form

$$\left[\delta\overline{\mathfrak{F}} \, X + \frac{1}{2} \delta\overline{\mathbb{F}} : (X \otimes X) - \delta\boldsymbol{F} \right] \rightarrow \left[\delta\overline{\boldsymbol{F}} + \delta\overline{\mathfrak{F}} \, X + \frac{1}{2} \delta\overline{\mathbb{F}} : (X \otimes X) - \delta\boldsymbol{F} \right]. \tag{D8}$$

Using once again a partial integration, the second term of (D1) is given by

$$\frac{1}{V} \int_{\mathcal{RVE}} \left[\overline{\mathfrak{P}}^{\mathfrak{B}} - \mathfrak{P} \right] \; \vdots \; \left[\delta\overline{\mathfrak{F}} + \delta\overline{\mathbb{F}} \, X - \delta\mathfrak{F} \right] dV$$

$$= \frac{1}{V} \int_{\mathcal{RVE}} \nabla \cdot \left(\left[\overline{\mathfrak{P}}^{\mathfrak{P}} - \mathfrak{P} \right]^{T1} : \left[\delta \overline{F} + \delta \overline{\mathfrak{F}} \, X + \frac{1}{2} \, \delta \overline{\mathbb{F}} : (X \otimes X) - \delta F \right] \right) \, \mathrm{d}V$$

$$+ \frac{1}{V} \int_{\mathcal{RVE}} \nabla \cdot \left([\nabla \cdot \mathfrak{P}]^{T} \left[\delta \overline{F} \, X + \frac{1}{2} \, \delta \overline{\mathfrak{F}} : (X \otimes X) + \frac{1}{6} \, \delta \overline{\mathbb{F}} \; \vdots \; (X \otimes X \otimes X) - \delta \varphi \right] \right) \, \mathrm{d}V$$

$$+ \frac{1}{V} \int_{\mathcal{RVE}} \nabla \cdot \nabla \cdot \mathfrak{P} \cdot \left[\delta \overline{F} \, X + \frac{1}{2} \, \delta \overline{\mathfrak{F}} : (X \otimes X) + \frac{1}{6} \, \delta \overline{\mathbb{F}} \; \vdots \; (X \otimes X \otimes X) - \delta \varphi \right] \, \mathrm{d}V. \tag{D9}$$

The introduction of the zero term leads to an easy summation of (D5) and (D9)

$$\frac{1}{V} \int_{\mathcal{RVE}} \left[\overline{P} - P \right] : \left[\delta \overline{F} + \delta \overline{\mathfrak{F}} \, X + \frac{1}{2} \, \delta \overline{\mathbb{F}} : (X \otimes X) - \delta F \right] \, \mathrm{d}V$$

$$+ \frac{1}{V} \int_{\mathcal{RVE}} \left[\overline{\mathfrak{P}}^{\mathfrak{P}} - \mathfrak{P} \right] \; \vdots \; \left[\delta \overline{\mathfrak{F}} + \delta \overline{\mathbb{F}} \, X - \delta \mathfrak{F} \right] \, \mathrm{d}V$$

$$= \frac{1}{V} \int_{\partial \mathcal{RVE}} \left(\left[\overline{P} - (P - \nabla \cdot \mathfrak{P}) \right] \, N \right) \cdot \left[\delta \overline{F} \, X + \frac{1}{2} \, \delta \overline{\mathfrak{F}} : (X \otimes X) \right.$$

$$\left. + \frac{1}{6} \, \delta \overline{\mathbb{F}} \; \vdots \; (X \otimes X \otimes X) - \delta \varphi \right] \, \mathrm{d}A$$

$$+ \frac{1}{V} \int_{\partial \mathcal{RVE}} \left(\left[\overline{\mathfrak{P}}^{\mathfrak{P}} - \mathfrak{P} \right] \, N \right) : \left[\delta \overline{F} + \delta \overline{\mathfrak{F}} \, X + \frac{1}{2} \, \delta \overline{\mathbb{F}} : (X \otimes X) - \delta F \right] \, \mathrm{d}A$$

$$+ \frac{1}{V} \int_{\mathcal{RVE}} \underbrace{\nabla \cdot (P - \nabla \cdot \mathfrak{P})}_{=0} \cdot \left[\delta \overline{F} \, X + \frac{1}{2} \, \delta \overline{\mathfrak{F}} : (X \otimes X) + \frac{1}{6} \, \delta \overline{\mathbb{F}} \; \vdots \; (X \otimes X \otimes X) - \delta \varphi \right] \, \mathrm{d}V, \tag{D10}$$

where we make use of the Gaussian integral theorem and the strong form of the microscopic continuum.

APPENDIX E. LINEARIZATION OF MACROSCOPIC STRESSES AND HYPERSTRESSES

The consistent linearization starts with the incremental macroscopic stresses and hyperstresses given by the correlated microscopic stresses and hyperstresses, see (17), which are inserted in the latter equation

$$\Delta \overline{P} = \frac{1}{V} \int_{\mathcal{RVE}} \Delta P \, \mathrm{d}V \quad \text{and} \quad \Delta \overline{\mathfrak{P}} = \frac{1}{V} \int_{\mathcal{RVE}} \Delta (P \otimes X + \mathfrak{P}) \, \mathrm{d}V. \tag{E1}$$

Since the microscopic stresses and hyperstresses depend on F and $\mathfrak{F}$, the chain rule is used

$$\left[\Delta \overline{P} \right]_{iJ} = \frac{1}{V} \int_{\mathcal{RVE}} \left([\mathbb{C}]_{iJsT} \, \Delta [F]_{sT} + [\mathsf{D}]_{iJsTU} \, \Delta \left[\mathfrak{F} \right]_{sTU} \right) \, \mathrm{d}V \, ,$$

$$\left[\Delta \overline{\mathfrak{P}} \right]_{iJK} = \frac{1}{V} \int_{\mathcal{RVE}} \left([\mathbb{C}]_{iJsT} \, [X]_K + [\mathsf{E}]_{iJKsT} \right) \, \Delta [F]_{sT} \, \mathrm{d}V \tag{E2}$$

$$+ \frac{1}{V} \int_{\mathcal{RVE}} \left([\mathsf{D}]_{iJsTU} \, [X]_K + [\mathsf{G}]_{iJKsTU} \right) \, \Delta \left[\mathfrak{F} \right]_{sTU} \, \mathrm{d}V.$$

The derivatives of the stresses with respect to the deformation tensors ($\mathbb{C}$, D, E, G) are defined in (29). The incremental microscopic deformation measures, see (12), are

$$\Delta [F]_{sT} = \Delta \left[\overline{F}\right]_{sT} + \Delta \left[\overline{\mathfrak{F}}\right]_{sTU} [X]_U + \Delta \left[\tilde{F}\right]_{sT} ,$$

$$\Delta \left[\mathfrak{F}\right]_{sTU} = \Delta \left[\overline{\mathfrak{F}}\right]_{sTU} + \Delta \left[\tilde{\mathfrak{F}}\right]_{sTU} ,$$

(E3)

compare (27) and (28).

APPENDIX F. APPROXIMATION OF MICROSCOPIC BOUNDARY VALUE PROBLEM

The domain of the representative volume element $\mathcal{RVE}$ is approximated by finite elements $\mathcal{RVE} \approx \mathcal{RVE}^h = \bigcup_{e=1}^{n} \mathcal{R}^e$ with the number of elements n. For the approximation of the microscopic boundary value problem (31) with the incremental deformation tensors of (32), we insert the approximations of (33) and (34)

$$\Delta G = \sum_{e=1}^{n} \left[\delta\tilde{q}\right]_i^{eA} \Bigg\{ \underbrace{\int_{\mathcal{R}^e} [\nabla R]_J^A \left[\mathbb{C}\right]_{iJsT}^{eh} dV \left[\Delta\overline{F}\right]_{sT}^e}_{[\mathfrak{L}_1]_{isT}^{eA}} + \underbrace{\int_{\mathcal{R}^e} [\nabla R]_J^A \left[\mathbb{C}\right]_{iJsT}^{eh} [X]_U^{eh} dV \left[\Delta\overline{\mathfrak{F}}\right]_{sTU}^e}_{[\mathbb{M}_1]_{isTU}^{eA}}$$

$$+ \underbrace{\int_{\mathcal{R}^e} [\nabla R]_J^A \left[\mathbb{C}\right]_{iJsT}^{eh} [\nabla R]_T^B dV \left[\Delta\tilde{q}\right]_s^{eB}}_{[K_1]_{is}^{eAB}} + \underbrace{\int_{\mathcal{R}^e} [\nabla R]_J^A [D]_{iJsTU}^{eh} dV \left[\Delta\overline{\mathfrak{F}}\right]_{sTU}^e}_{[\mathbb{M}_2]_{isTU}^{eA}}$$

$$+ \underbrace{\int_{\mathcal{R}^e} [\nabla R]_J^A [D]_{iJsTU}^{eh} [\nabla^2 R]_{TU}^B dV \left[\Delta\tilde{q}\right]_s^{eB}}_{[K_2]_{is}^{eAB}} + \underbrace{\int_{\mathcal{R}^e} [\nabla^2 R]_{JK}^A [E]_{iJKsT}^{eh} dV \left[\Delta\overline{F}\right]_{sT}^e}_{[\mathfrak{L}_2]_{isT}^{eA}}$$

$$+ \underbrace{\int_{\mathcal{R}^e} [\nabla^2 R]_{JK}^A [E]_{iJKsT}^{eh} [X]_U^{eh} dV \left[\Delta\overline{\mathfrak{F}}\right]_{sTU}^e}_{[\mathbb{M}_3]_{isTU}^{eA}} + \underbrace{\int_{\mathcal{R}^e} [\nabla^2 R]_{JK}^A [E]_{iJKsT}^{eh} [\nabla R]_T^B dV \left[\Delta\tilde{q}\right]_s^{eB}}_{[K_3]_{is}^{eAB}}$$

(F1)

$$+ \underbrace{\int_{\mathcal{R}^e} [\nabla^2 R]_{JK}^A [G]_{iJKsTU}^{eh} dV \left[\Delta\overline{\mathfrak{F}}\right]_{sTU}^e}_{[\mathbb{M}_4]_{isTU}^{eA}} + \underbrace{\int_{\mathcal{R}^e} [\nabla^2 R]_{JK}^A [G]_{iJKsTU}^{eh} [\nabla^2 R]_{TU}^B dV \left[\Delta\tilde{q}\right]_s^{eB}}_{[K_4]_{is}^{eAB}} \Bigg\}.$$

(F1)

In the end, we can write

$$\Delta G = \sum_{e=1}^{n} \left[\delta\tilde{q}\right]_i^{eA} \left\{ [K]_{is}^{eAB} \left[\Delta\tilde{q}\right]_s^{eB} + [\mathfrak{L}]_{isT}^{eA} \left[\Delta\overline{F}\right]_{sT}^e + [\mathbb{M}]_{isTU}^{eA} \left[\Delta\overline{\mathfrak{F}}\right]_{sTU}^e \right\}$$

(F2)

with

$$[K]_{is}^{eAB} = [K_1]_{is}^{eAB} + [K_2]_{is}^{eAB} + [K_3]_{is}^{eAB} + [K_4]_{is}^{eAB},$$

$$[\mathfrak{L}]_{isT}^{eA} = [\mathfrak{L}_1]_{isT}^{eA} + [\mathfrak{L}_2]_{isT}^{eA},$$

$$[\mathbb{M}]_{isTU}^{eA} = [\mathbb{M}_1]_{isTU}^{eA} + [\mathbb{M}_2]_{isTU}^{eA} + [\mathbb{M}_3]_{isTU}^{eA} + [\mathbb{M}_4]_{isTU}^{eA}.$$

(F3)

After assembling over all elements with $(\bullet) = A_{e=1}^{n} (\bullet)e$, we get in the equilibrium state

$$\Delta G = \left[\delta\tilde{\boldsymbol{q}}\right]_i^A \left\{ [\boldsymbol{K}]_{is}^{AB} \left[\Delta\tilde{\boldsymbol{q}}\right]_s^B + [\mathfrak{L}]_{isT}^A \left[\Delta\overline{\boldsymbol{F}}\right]_{sT} + [\mathbb{M}]_{isTU}^A \left[\Delta\overline{\mathfrak{F}}\right]_{sTU} \right\}. \tag{F4}$$

Thus, using $\Delta G = 0$, the correlation between the sensitivities and the change of corresponding macroscopic fields is given in the discrete setting as follows

$$\left[\Delta\tilde{\boldsymbol{q}}\right]_s^B = -\left([\boldsymbol{K}]_{ls}^{AB}\right)^{-1} \left([\mathfrak{L}]_{lrT}^A \left[\Delta\overline{\boldsymbol{F}}\right]_{rT} + [\mathbb{M}]_{lrTU}^A \left[\Delta\overline{\mathfrak{F}}\right]_{rTU} \right). \tag{F5}$$

APPENDIX G. APPROXIMATION OF MACROSCOPIC STRESSES

In this section, we derive the discretized macroscopic stresses. We start with the discretization of the linearization of $\overline{\boldsymbol{P}}$:

$$\left[\Delta\overline{\boldsymbol{P}}\right]_{iJ}^h = \left[\mathbb{V}^{\mathbb{C}}\right]_{iJsT}^h \left[\Delta\overline{\boldsymbol{F}}\right]_{sT} + \left[\mathbb{V}^{\mathbb{CD}}\right]_{iJsTU}^h \left[\Delta\overline{\mathfrak{F}}\right]_{sTU} + [\mathfrak{N}]_{iJs}^B \left[\Delta\tilde{\boldsymbol{q}}\right]_s^B, \tag{G1}$$

with the volume-averaged tensors

$$\left[\mathbb{V}^{\mathbb{C}}\right]_{iJsT}^h = \frac{1}{V} \int\limits_{\mathcal{RVE}^h} [\mathbb{C}]_{iJsT}^h \, \mathrm{d}V,$$

$$\left[\mathbb{V}^{\mathbb{CD}}\right]_{iJsTU}^h = \frac{1}{V} \int\limits_{\mathcal{RVE}^h} \left([\mathbb{C}]_{iJsT}^h [\boldsymbol{X}]_U^h + [\mathrm{D}]_{iJsTU}^h \right) \mathrm{d}V, \tag{G2}$$

$$[\mathfrak{N}]_{iJs}^B = \frac{1}{V} \int\limits_{\mathcal{RVE}^h} \left([\mathbb{C}]_{iJsT}^h [\nabla R]_T^B + [\mathrm{D}]_{iJsTU}^h \left[\nabla^2 R\right]_{TU}^B \right) \mathrm{d}V.$$

Inserting the discrete sensitivities (F5) yields

$$\left[\Delta\overline{\boldsymbol{P}}\right]_{iJ}^h = \left\{ \left[\mathbb{V}^{\mathbb{C}}\right]_{iJrT}^h - [\mathfrak{N}]_{iJs}^B \left([\boldsymbol{K}]_{ls}^{AB}\right)^{-1} [\mathfrak{L}]_{lrT}^A \right\} \left[\Delta\overline{\boldsymbol{F}}\right]_{rT}$$
$$+ \left\{ \left[\mathbb{V}^{\mathbb{CD}}\right]_{iJrTU}^h - [\mathfrak{N}]_{iJs}^B \left([\boldsymbol{K}]_{ls}^{AB}\right)^{-1} [\mathbb{M}]_{lrTU}^A \right\} \left[\Delta\overline{\mathfrak{F}}\right]_{rTU}. \tag{G3}$$

Furthermore, we discretize the linearization of the hyperstresses $\overline{\mathfrak{P}}$

$$\left[\Delta\overline{\mathfrak{P}}\right]_{iJK}^h = \left[\mathbb{V}^{\mathbb{CE}}\right]_{iJKsT}^h \left[\Delta\overline{\boldsymbol{F}}\right]_{sT} + \left[\mathbb{V}^{\mathbb{CDEG}}\right]_{iJKsTU}^h \left[\Delta\overline{\mathfrak{F}}\right]_{sTU} + [\mathbb{N}]_{iJKs}^B \left[\Delta\tilde{\boldsymbol{q}}\right]_s^B, \tag{G4}$$

with the volume-averaged tensors

$$\left[\mathbb{V}^{\mathbb{CE}}\right]_{iJKsT}^h = \frac{1}{V} \int\limits_{\mathcal{RVE}^h} \left([\mathbb{C}]_{iJsT}^h [\boldsymbol{X}]_K^h + [\mathrm{E}]_{iJKsT}^h \right) \mathrm{d}V,$$

$$\left[\mathbb{V}^{\mathbb{CDEG}}\right]_{iJKsTU}^h = \frac{1}{V} \int\limits_{\mathcal{RVE}^h} \left([\mathbb{C}]_{iJsT}^h [\boldsymbol{X}]_K^h [\boldsymbol{X}]_U^h + [\mathrm{D}]_{iJsTU}^h [\boldsymbol{X}]_K^h \right.$$
$$\left. + [\mathrm{E}]_{iJKsT}^h [\boldsymbol{X}]_U^h + [\mathrm{G}]_{iJKsTU}^h \right) \mathrm{d}V,$$

$$[\mathbb{N}]_{iJKs}^B = \frac{1}{V} \int\limits_{\mathcal{RVE}^h} \left([\mathbb{C}]_{iJsT}^h [\boldsymbol{X}]_K^h + [\mathrm{E}]_{iJKsT}^h \right) [\nabla R]_T^B \, \mathrm{d}V$$

$$+ \frac{1}{V} \int\limits_{\mathcal{RVE}^h} \left([\mathrm{D}]_{iJsTU}^h [\boldsymbol{X}]_K^h + [\mathrm{G}]_{iJKsTU}^h \right) \left[\nabla^2 R\right]_{TU}^B \Bigg\} \, \mathrm{d}V. \tag{G5}$$

Insertion once again of the discrete sensitivities (F5) yields

$$\left[\Delta\overline{\mathfrak{P}}\right]_{iJK}^{\mathrm{h}} = \left\{ \left[\mathbb{V}^{\mathbb{C}\mathbb{E}}\right]_{iJKrT}^{\mathrm{h}} - \left[\mathbb{N}\right]_{iJKs}^{B} \left(\left[\boldsymbol{K}\right]_{ls}^{AB}\right)^{-1} \left[\mathfrak{L}\right]_{lrT}^{A} \right\} \left[\Delta\overline{\boldsymbol{F}}\right]_{rT}$$
$$+ \left\{ \left[\mathbb{V}^{\mathbb{C}\mathbb{D}\mathbb{E}\mathbb{G}}\right]_{iJKrTU}^{\mathrm{h}} - \left[\mathbb{N}\right]_{iJKs}^{B} \left(\left[\boldsymbol{K}\right]_{ls}^{AB}\right)^{-1} \left[\mathbb{M}\right]_{lrTU}^{A} \right\} \left[\Delta\overline{\mathfrak{F}}\right]_{rTU}. \tag{G6}$$